

A Laser-Assisted Microchemistry System for the Fabrication of Small Electromechanical Devices

by

Nick I. Nassuphis

B.S., National Technical University of Athens (1991)

Submitted to the Department of Mechanical Engineering
in partial fulfillment of the requirements for the degree of

Master of Science

at the

MASSACHUSETTS INSTITUTE OF TECHNOLOGY

February 1994

© Massachusetts Institute of Technology 1994. All rights reserved.

Author /NICK NASSUPHIS.....

Department of Mechanical Engineering

January 24, 1994

Certified by D.J. Ehrlich

D.J. Ehrlich

Senior Staff, Lincoln Laboratory
Thesis Supervisor

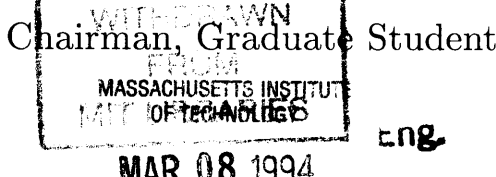
Certified by A. Slocum

A. Slocum

Associate Professor, Department of Mechanical Engineering
A. Slocum
Thesis Supervisor

Accepted by A. Sonin

A. Sonin



A Laser-Assisted Microchemistry System for the Fabrication of Small Electromechanical Devices

by

N. I. Nassuphis

Submitted to the Department of Mechanical Engineering
on January 24, 1994, in partial fulfillment of the
requirements for the degree of
Master of Science

Abstract

Laser microchemical technology offers processes for one-step laser chemical vapor deposition, one step disconnect, and one-step via formation. Metallization writing rates for 1- to 5- μm -thick conductors are usually 50 to 1000 $\mu\text{m}/\text{s}$. Resistivities are typically 3-15 $\mu\Omega \text{ cm}$ for many metals (e.g. Pt, Al, Cu, Au, W, and Co). Processes have been developed to include metallurgies for multichip modules and microelectromechanical devices (MEM).

The laser microchemical technology has been previously shown to be capable of 0.5- μm linewidth and writing speeds up to 2 mm/s . A system consistent with these capabilities was constructed in order to implement the technology. The X-Y, motion is servo-controlled to a 0.25 μm resolution over a 6-inch range of travel; Z is controlled to 0.1 μm . Three-axis motion is synchronized with laser operations by means of a dedicated microprocessor. Laser parameters and motion paths are specified on a live video image of the workpiece by means of an interactive graphical user interface. Three-dimensional contouring is achieved by approximating the spot trajectory as a sequence of X-Y-Z target points connected by linear, constant velocity motion paths. Laser power, repetition rate and scan velocity can be varied arbitrarily as the path is traversed. Proper workpiece alignment and process repeatability are achieved with image-based positioning and calibration algorithms. Path editing features, store and load capability and process parameter libraries allow automation of the processing routines.

The occurrence of periodic morphologies for certain process parameters was investigated and a model to explain these observations was formulated. Numerical simulation using the formulated model reproduced the observed morphological structures.

System capabilities were demonstrated on integrated circuits (ICs), multichip modules (MCMs) and MEM devices. It was found that the high resolution is essential for ICs, while the three dimensional capability is needed for MCMs and MEMs. Laser-deposited copper, aluminum, platinum and gold conductors were developed. The

processes permit real-time writing of interconnection for circuit configuration, rework, chip bondout, testing and systems engineering. Recent process extensions now permit operation on MCM metallurgies including all silicon, ceramic, and advanced deposited layer or laminate technologies. Collaborative demonstrations have been completed with several MCM foundries. The technology was found to provide (1) a low-cost rework option, (2) reversible interconnect for module testing, (3) means to implement redundancy and universal substrate options, and (4) means to trim terminations and other circuit parameters. Furthermore, it permits circuit configuration directly from the CAD environment with no hard tooling, and thereby shortens the MCM or IC development cycle. In the MEM application, real-time tuning of device parameters under live test has been demonstrated.

Thesis Supervisor: D.J. Ehrlich
Title: Senior Staff, Lincoln Laboratory

Thesis Supervisor: A. Slocum
Title: Associate Professor, Department of Mechanical Engineering

Acknowledgments

I would like to thank Dan Ehrlich, Steve Palmacci, Ted Bloomstein and Rick Mathews. Their help is greatly appreciated.

Contents

1	Introduction	7
1.1	System	8
1.2	Processes	12
1.3	Software	13
1.4	Electronics Applications	14
1.5	Mechanics Applications	16
2	Experiments	19
2.1	Molybdenum	24
2.2	Platinum	29
2.3	Discussion	33
3	Applications	36
3.1	A typical modification sequence	36
3.2	A Severed Wire is Reconnected	39
3.3	A Staircase Via	40
3.4	Low-resistance platinum-to-copper contacts	41
3.5	Depassivation	42
4	Modeling	44
4.1	Analytical Solutions	45
4.2	Green's Function derivation	46
4.3	Numerical Solutions	53
4.4	A finite difference scheme for the 3D unsteady case	54

4.5	Implementation of the 3D, unsteady heat diffusion solver	59
4.6	Deposition	61
4.7	Deposition : Implementation	65
4.8	Deposition : Results	66
4.9	The fully coupled case	68
4.10	Code Listing	71
5	Conclusions	78
5.1	Summary	78
5.2	Refrences	80

Chapter 1

Introduction

Recent advances in the design of microelectronics and micromechanics have resulted in an increased demand for fast prototyping of complex micro devices. The lithographic techniques used to fabricate these devices are very suitable for mass production at low unit costs. They do not, however, offer the low volume prototyping capabilities needed during the initial design stage. There are very few single-step manufacturing processes that can be used at the micro scale for the construction of devices for testing, repair or experimentation purposes. One way to achieve localized chemical processing is to employ an energy source that is *spatially confined*, such as a *focused laser beam*. Use of such an energy source localizes the reaction to length scales dictated by heat and mass transport in the region around the laser spot.¹ One application of this concept is the deposition of metals by *pyrolytic decomposition* of gaseous organometallic compounds. Another use is the selective material removal through *laser-activated etching* of the substrate.²

¹ Bertolotti (ed.): “Physical Processes in Laser-Materials Interactions” (Plenum Press, 1983)

² D.J. Ehrlich and A. Tsao (eds.): “Laser Microfabrication” (Academic Press, 1988)

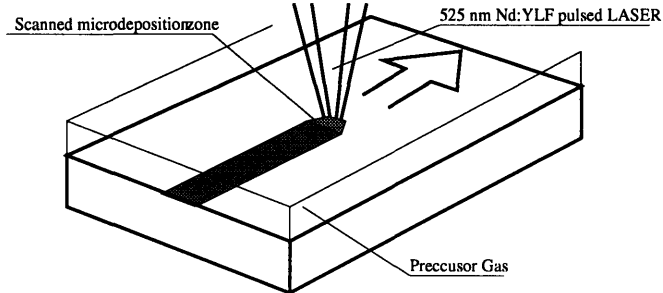


Figure 1.1 : In laser-assisted microchemical processing, the focused laser heats the substrate and so activates the reaction used to locally deposit, etch or otherwise modify the substrate.

The other technology suitable for micro-scale machining is focused ion beam processing, which can also be used for material removal or deposition. The ion beam technique has a higher spatial resolution because it is not limited by the diffraction of the (relatively) long wavelength of light. The disadvantage of ion-beam processing is the low throughput, which typically is on the order of minutes per μm of deposited material. For most applications under consideration, this translates into unacceptably long times.

This work focused on the development of a laser-driven microchemistry system for the fabrication of small electronic and mechanical systems. A significant fraction of the effort went into the development of the actual system, both hardware and software. Process characterization experiments were performed, and a number of “real-life” repair jobs were completed. Procedures to address the fabrication of specific microstructures were developed. The deposition process itself was studied and a model was developed to explain periodic structures occurring for certain operating conditions. Numerical simulations based on the model produced the experimentally observed structures, thus supporting the assumptions on which the model was based.

1.1 System

An integrated laser microchemistry system was built in order to investigate the usefulness of the process for the manufacturing and modification of electrical and mechanical microdevices. (figure 1.2)

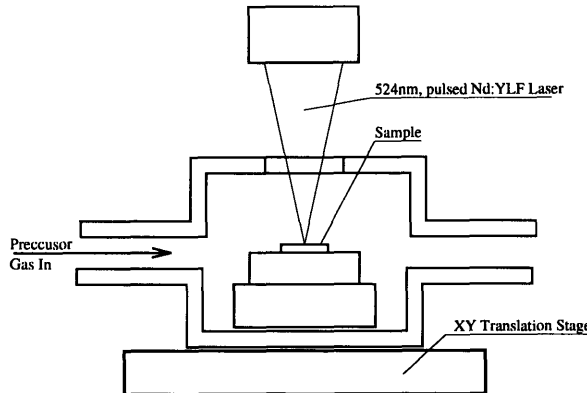


Figure 1.2 : The main components of the LCVD system built

The system is driven by a motion controller and a personal computer running an automated, interactive, graphical interface that integrates all subsystems into a usable laser microchemical processing system.

A number of chemistries were investigated for their applicability and their performance with various substrates was characterized. The system itself was used extensively for real chip repairs and trimming of micromechanical devices. Most of the work was focused on the deposition of metals and laser ablation, but chlorine etching of silicon was also demonstrated.

The repair “case-studies” revealed a number of process control and automation issues that had to be resolved for the system to realize its potential as a tool for fast, single-unit microfabrication.

The system comprises the following subunits:

- 524 nm, frequency-doubled, pulsed, diode-pumped Nd:YLF laser.
- XY translation stage with $0.2 \mu\text{m}$ positioning accuracy over a six inch travel.
- $0.1 \mu\text{m}$ accuracy, 1-inch-travel Z axis on which to move the focal point.
- 0.5 numerical aperture laser focusing optics.
- Vacuum subsystem.
- 4-axis motion controller.

- Timer, digital and analog I/O boards.
- PC running a graphical user interface.
- Supporting electronics, sensors and actuators.

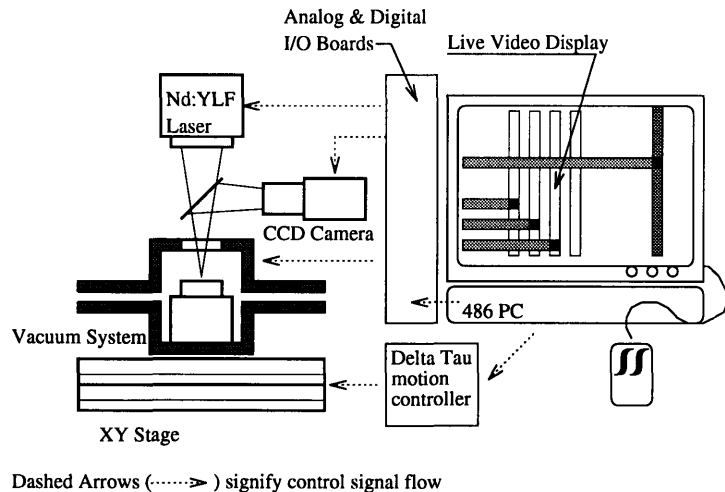


Figure 1.3 : The subsystems comprising the laser-assisted microchemistry system built

The system is mounted on a frame with a passive vibration isolation mechanism. A monitor, mouse and keyboard used to control system operations is attached externally. Figure 1.4 shows the system without its protective skin.

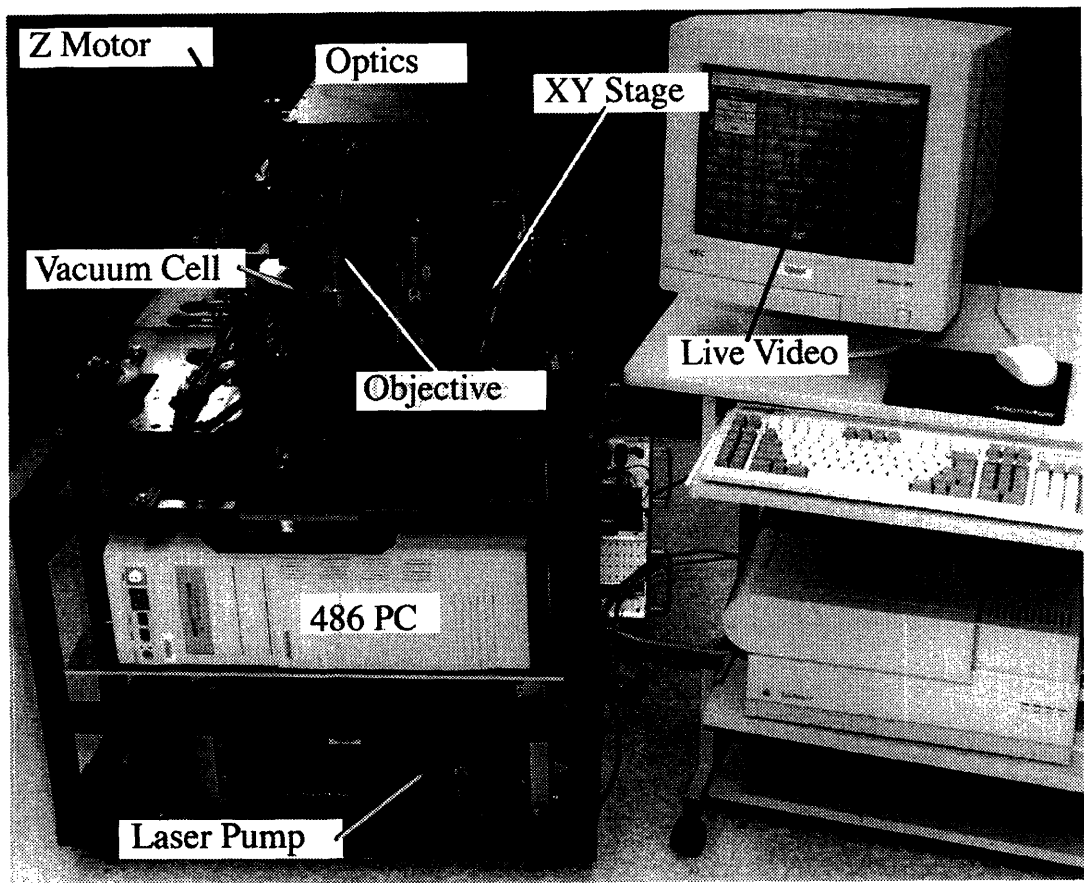


Figure 1.4 : The laser microchemistry system and its components

1.2 Processes

A number of different precursors and substrates were used in conjunction with the described system. The materials that were successfully deposited include platinum, aluminum, copper, molybdenum, gold and silicon. Silicon etching with chlorine was also demonstrated. Vacuum operation results in material removal through ablation. The following table lists the achievable spatial resolution, deposition speed and physical properties for the metals that the system can handle.

Compound	Material	Geometry	Resistivity	Speed
Silicon	Low Stress Microcrystalline	0.2 - 20 μm wide	1 mOhm-cm	1000 $\mu\text{m}/\text{s}$
	Polycrystalline	0.1-20 μm thick		
	Low Stress alpha-phase	2 - 20 μm wide 0.1-4 μm thick		
Tungsten	Microcrystalline	1 - 10 μm wide	12-25 $\mu\text{Ohm-cm}$	200 $\mu\text{m}/\text{s}$
	Polycrystalline	0.1-20 μm thick		
Nickel	Microcrystalline	1 - 25 μm wide	17-70 $\mu\text{Ohm-cm}$	200 $\mu\text{m}/\text{s}$
	Polycrystalline	0.1-2 μm thick		
Cobalt	Microcrystalline	0.1-2 μm thick	13-25 $\mu\text{Ohm-cm}$	50 $\mu\text{m}/\text{s}$
Platinum	Microcrystalline	0.5 - 8 μm wide 0.1-15 μm thick	11-15 $\mu\text{Ohm-cm}$	200 $\mu\text{m}/\text{s}$
Aluminum	Microcrystalline	0.5 - 10 μm wide	4 $\mu\text{Ohm-cm}$	200 $\mu\text{m}/\text{s}$
	Polycrystalline	0.1-4 μm thick		
Copper	Microcrystalline	0.5 - 10 μm wide	7 $\mu\text{Ohm-cm}$	10 $\mu\text{m}/\text{s}$
	Polycrystalline	0.1-10 μm thick		
Molybdenum	Microcrystalline	0.5 - 15 μm wide 0.1-10 μm thick	24 $\mu\text{Ohm-cm}$	100 $\mu\text{m}/\text{s}$
Gold	Polycrystalline	0.5 - 20 μm wide 0.1 - 10 μm thick	3 $\mu\text{Ohm-cm}$	10 $\mu\text{m}/\text{s}$

Figure 1.5 : Demonstrated deposition chemistries.

The versatility of the LCVD system is evident from figure 1.5, which list the deposition chemistries that were demonstrated on the system. Etching and ablation further add to the spectrum of available processes, making LCVD usable for a wide range of applications.

1.3 Software

User interaction with the device is directed through a live video image that is digitized directly from the optics subsystem. Positioning to device features is done by “point-and-click” and results of processing operations are immediately visible on the display.

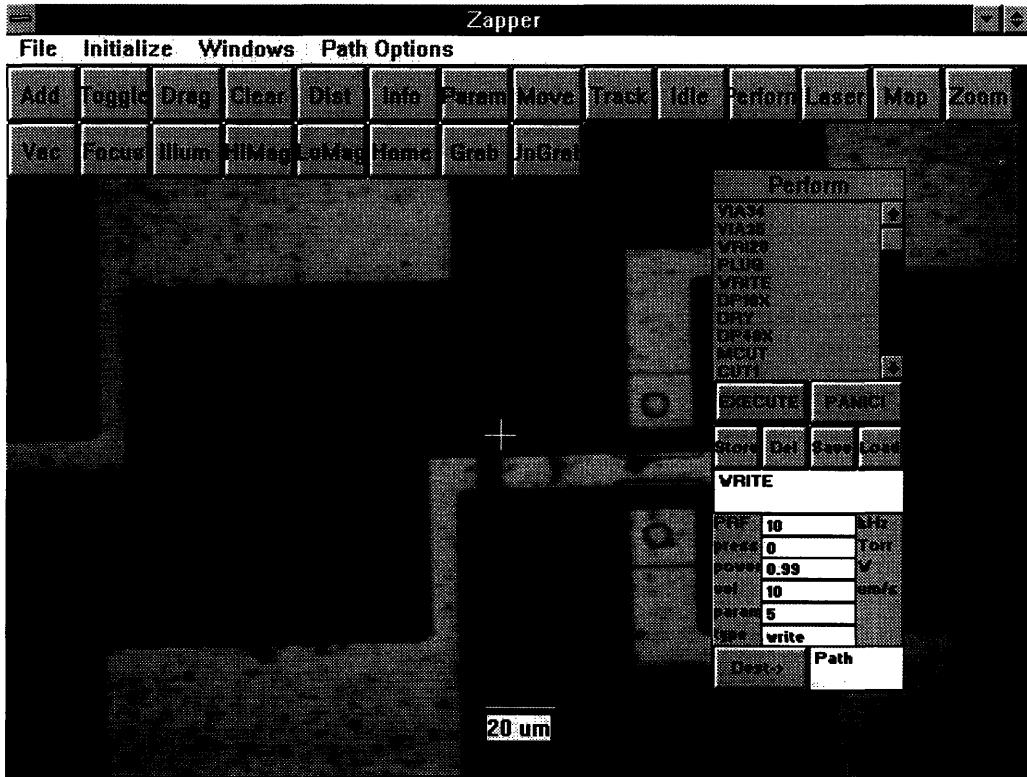


Figure 1.6 : Typical system display. Note the live video and the graphical control elements

Real-time monitoring of device performance is used to achieve precise trimming of electronic or mechanical devices. A number of highly calibrated analog microsensors were fabricated using this approach. The driving software provides all the necessary “hook’s” for closed-loop operation of this type.

The system can be externally driven through an ethernet connection to a workstation running industry standard CAD software. This allows digital design and chip layout information to be used for system positioning and operation purposes. Processing schedules can also be extracted from CAD data files, allowing system users to specify operations through a familiar design interface.

1.4 Electronics Applications

The electronics applications of the system center around rewiring of microelectronic prototypes in order to avoid costly and time-consuming batch fabrication. Wires can be added to or removed from the circuitry using the laser-driven microchemical reactions.

The steps needed to create a conductive path are shown in figure 1.7

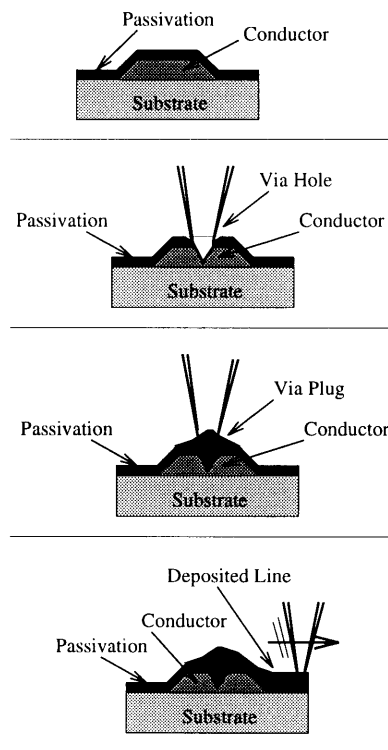


Figure 1.7: creation of an electrical contact to a wire below a layer of passivation using a combination of laser ablation and laser-driven deposition

A $1.5 \mu\text{m}$ platinum conductor deposited on top of the passivation layer is shown in figure 1.8. Note that only the endpoints of the deposited conductor are in electrical contact with the wire under the passivation.

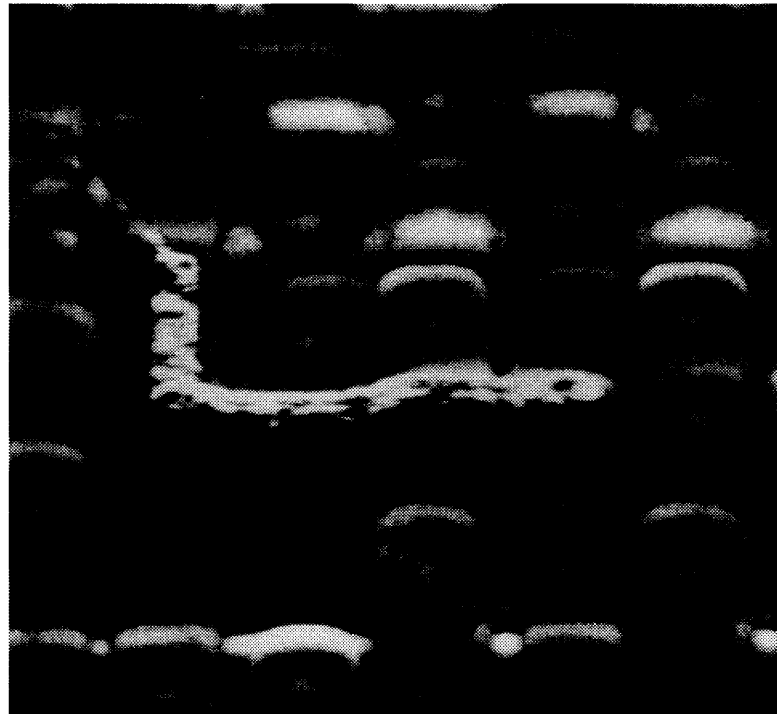


Figure 1.8 : 1.5 μm platinum line deposited on a layer passivation.

The wires below the endpoints are electrically connected

1.5 Mechanics Applications

Micromechanical applications of the system exploit the mechanical properties of the deposited material along with the system's spatial resolution.

An ideal test-case was an on-chip micro-sensor which uses an actively driven proof mass to measure angular acceleration. Imperfect balancing of the proof mass limits the accuracy of the device. These fabrication errors could not be corrected because there is no machining capability suited to the size of the device. (the proof mass is about 200 by 100 μm wide and 2 μm thick)

The mass is excited by interdigitated electrostatic actuators, and its response is measured by a capacitive sensor approx. 5 μm below the suspended mass. This geometry precludes the use of any machining technique that would cause significant contact forces.

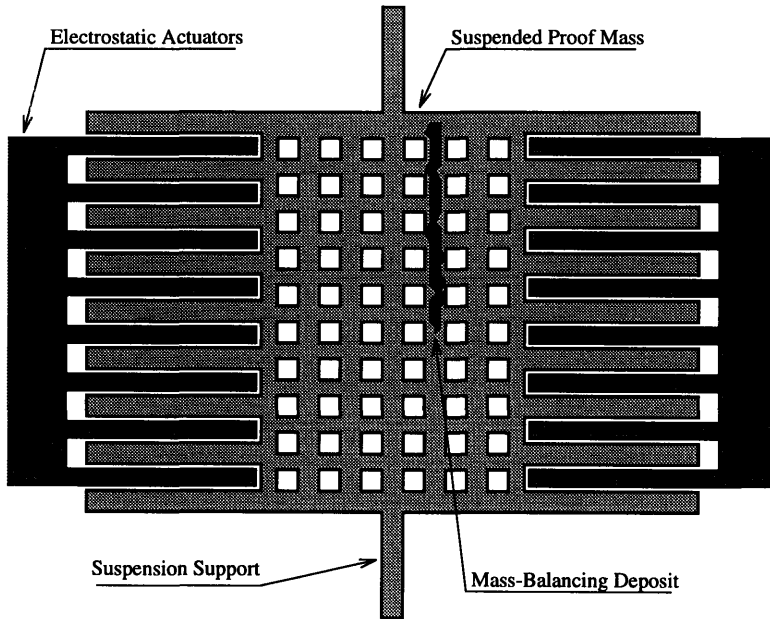


Figure 1.9 : The electrostatically driven proof mass of the microsensor.

Laser-driven microdeposition has the high spatial resolution
and the low contact forces needed to successfully trim this device.

Figure 1.10 is an enlargement of the area surrounded by the dashed line in figure 1.9. Note the regular pattern of openings on the proof mass, which is designed to minimize

the viscous damping due to residual gas between the surface of the capacitive sensor and the suspended mass.

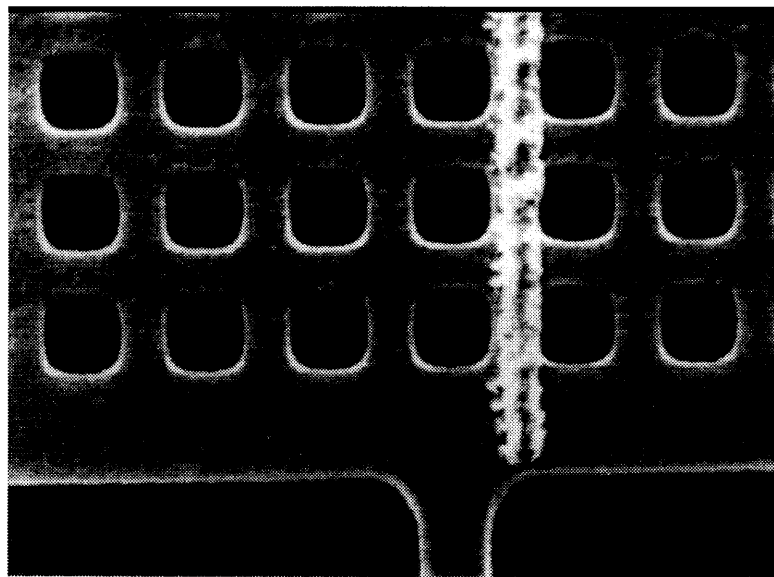


Figure 1.10 : Platinum deposit nulls sensor error.

Measurement of the sensor's error while mass is deposited allows closed loop trimming resulting in near-perfect device response. The "closed loop" trimming operation could be automated and incorporated into a mass manufacturing process.

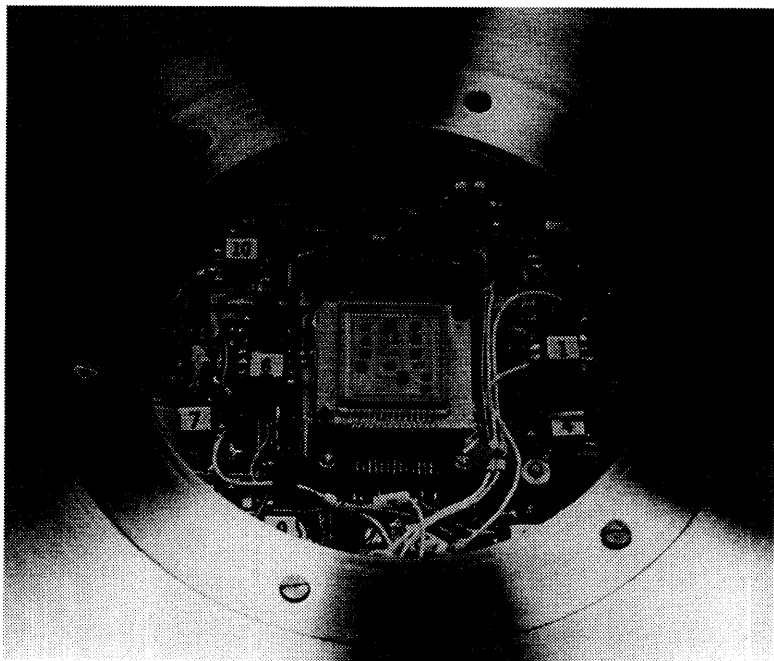


Figure 1.11 : The microsensor in the LCVD cell with

the control and measurement electronics

This is an application for which laser-driven microdeposition is ideally suited. There is no alternative trimming method offering the same repeatability, throughput and convenience. There seems to be significant potential for the application of laser-assisted CVD towards the solution of this class of microfabrication problems.

Chapter 2

Experiments

A thorough characterization of the properties of laser-deposited metals is necessary in order to use the system in the most effective way. The deposit properties that are most important for microelectronic rewiring are contact resistance, resistivity and crosssectional area. The laser-driven CVD experiments were performed using a CW Argon and a Pulsed Nd:YLF laser. Metals deposited include platinum, gold, copper and aluminum on silicon, silicon oxide and polyimide substrates.

The process parameters examined were:

- Laser Power
- Q-Switch Rep Rate
- Scanning Speed
- Precursor Pressure
- Number of Passes

The cross-sectional area of the deposit was measured using a contact probe profilometer. Resistance was obtained using a four-point-probe.

The driving software was used to generate the S-shaped paths that vary the particular process parameter under investigation during the characterization experiment.

The software compensates for substrate tilt by interpolating Z values between the endpoints of the path. A flatness compensation strategy of this type is essential for repeatability because of process sensitivity to energy density variations. The narrow depth of focus (1 μm for the 40X objective) causes significant energy density variations for small Z displacements from the optimal focal point.

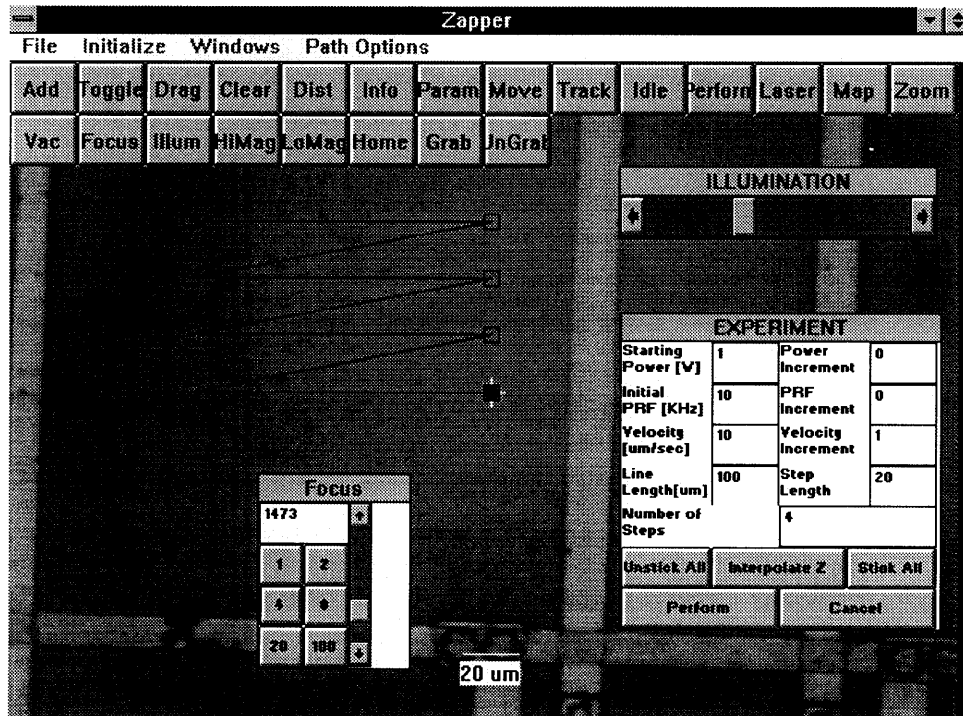


Figure 2.1 : The software automatically generates the XYZ path and the process parameters for a characterization experiment

A typical deposition experiment would, for example, involve the deposition of Pt on Polyimide using the CW Argon laser. Figures 2.2 to 2.5 show SEMs of such a process characterization experiment.

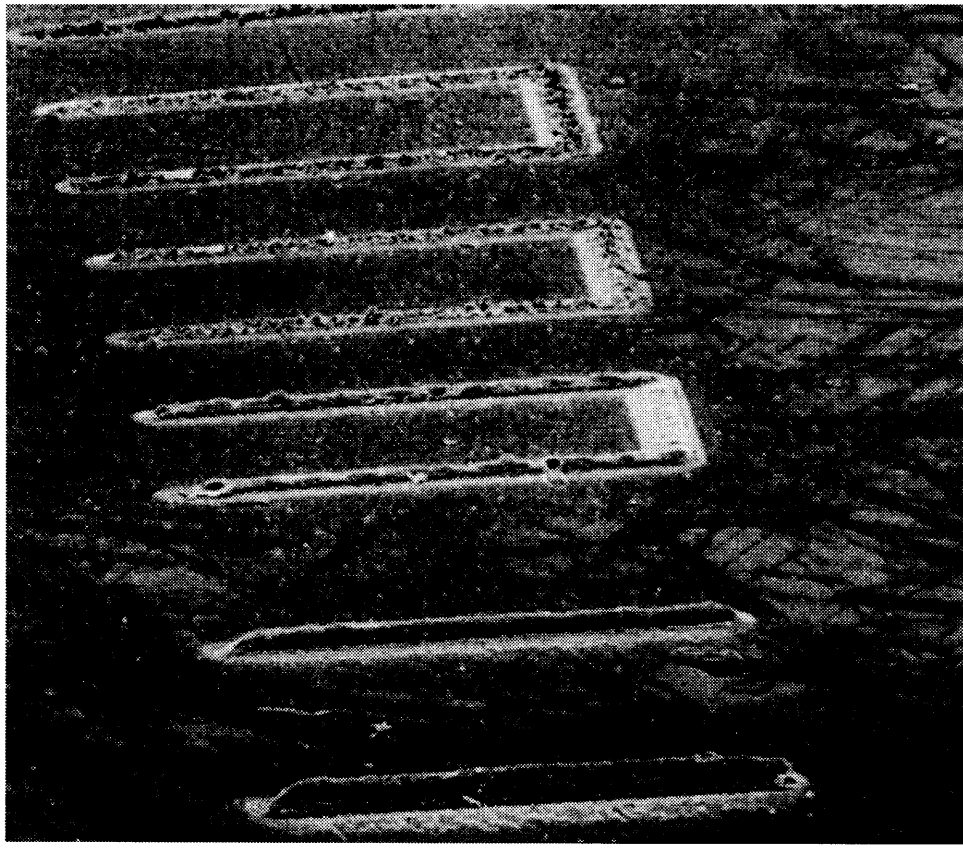


Figure 2.2 : Platinum lines written on Polyimide substrate
1 $\mu\text{m}/\text{s}$ up to 2000 $\mu\text{m}/\text{s}$ deposition speed, 593 mW laser power
5 KHz pulse rate and 3 Torr precursor pressure

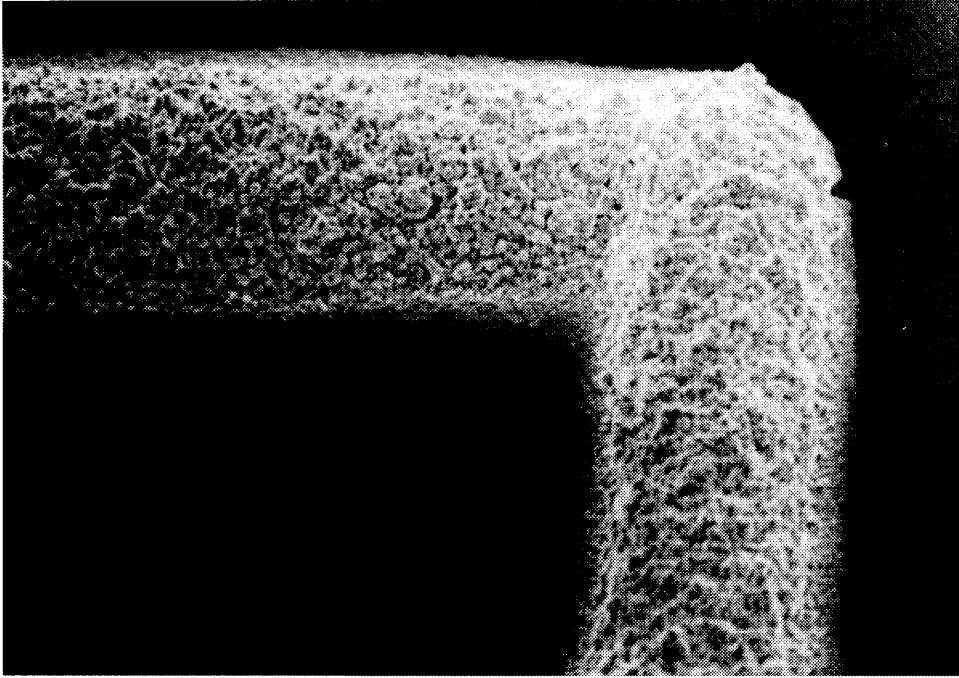


Figure 2.3 : Platinum line written on Polyimide substrate
one pass, $1 \mu\text{m}/\text{s}$ at 5 KHz and 593 mW

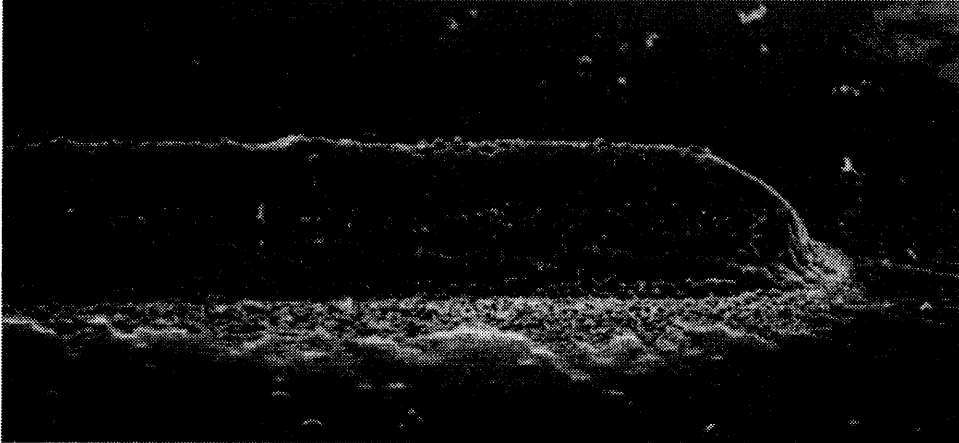


Figure 2.4 : Platinum line on Polyimide substrate.
16 passes, $2 \mu\text{m}/\text{s}$ writing speed at 5 KHz and 593 mW

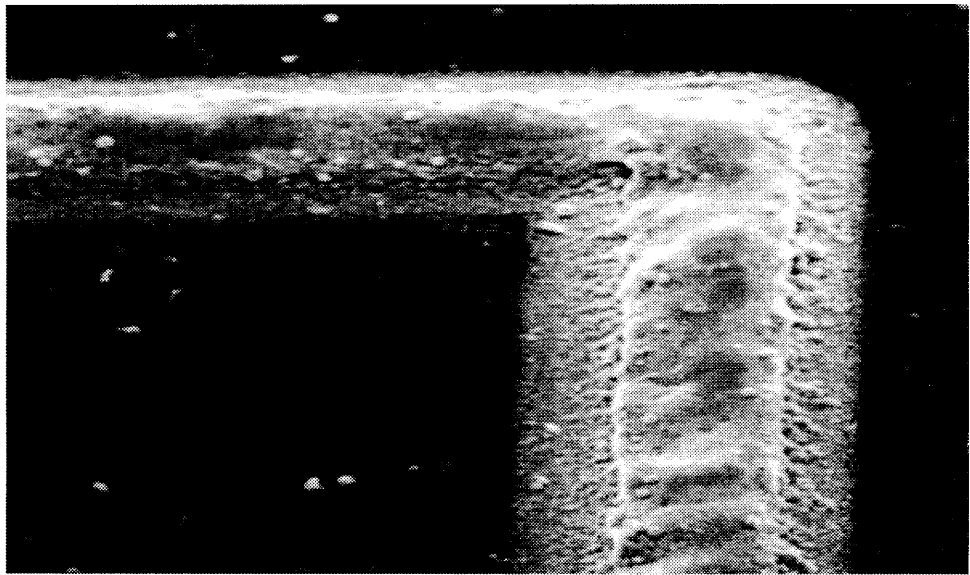


Figure 2.5 : Platinum line on Polyimide substrate

8 passes, $100 \mu\text{m}/\text{s}$ writing speed at 5 KHz and 593 mW

2.1 Molybdenum

Figure 2.6 shows the resistance of laser-deposited molybdenum lines as a function of writing speed and laser power. The CW Argon laser was pumped at powers ranging from 40mW up to 200 mW, while the XY stage was scanned from $1 \mu\text{m}/\text{s}$ up to $2000 \mu\text{m}/\text{s}$.

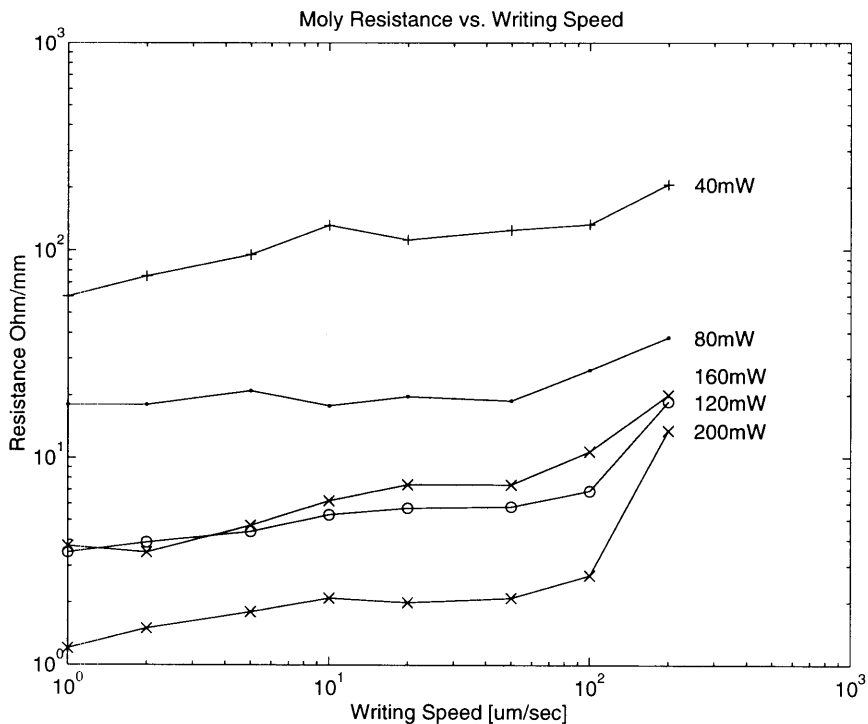


Figure 2.6 : Molybdenum line resistance [Ω / mm] as a function of writing speed [$\mu\text{m}/\text{s}$] using a CW Argon Laser.

Line resistance increases for increasing scanning speeds, as it did for the copper deposit. There does not appear to be a clearly defined “saturation” speed. Again, resistance decreases as laser power increases. The resistance observed is a function of the geometry of the deposited line and the material’s resistivity. In order to separate the two effects, line dimensions were measured using a contact probe profilometer. The measurements are shown in figures 2.7 and 2.8.

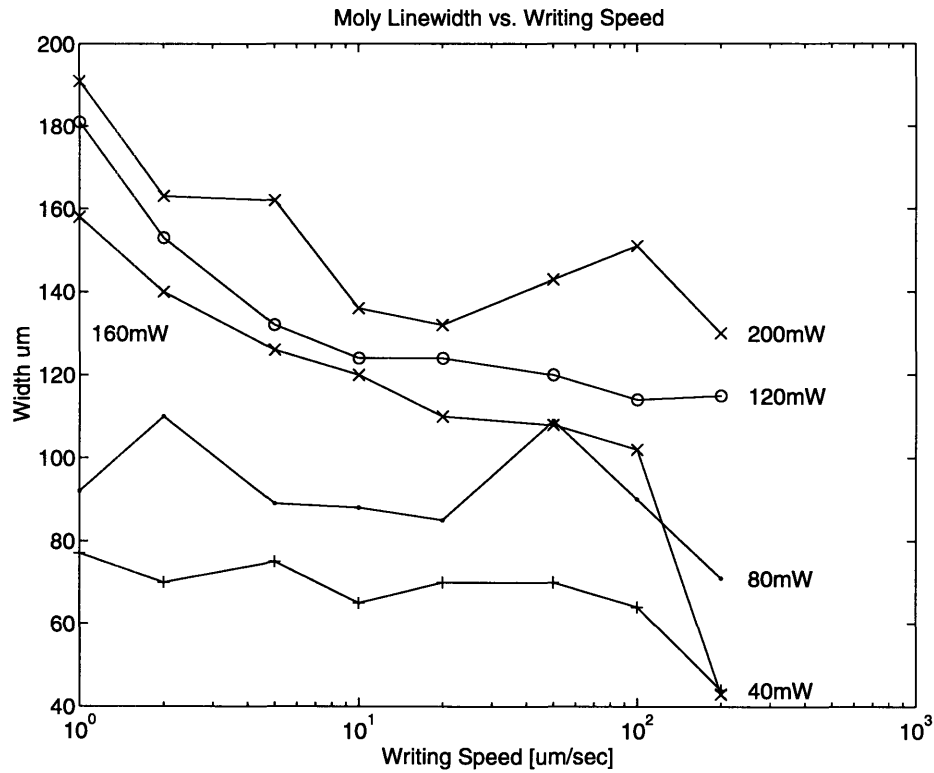


Figure 2.7 : Molybdenum line width [μm] as a function of writing speed [$\mu\text{m/s}$] using a CW Argon Laser.

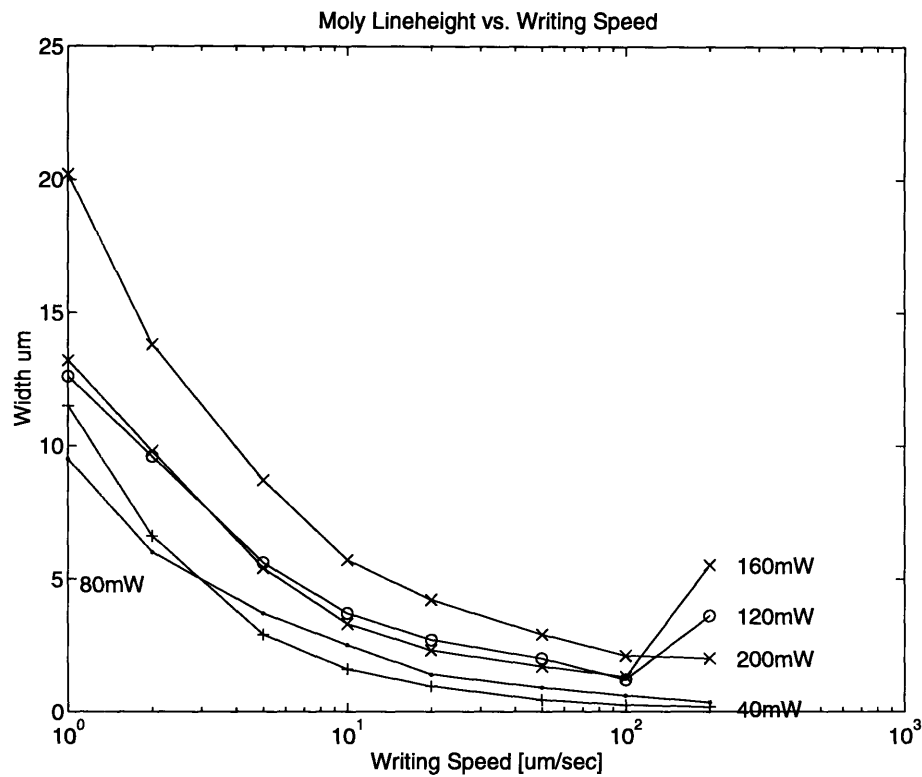


Figure 2.8 : Molybdenum line height [μm] as a function of writing speed [$\mu\text{m}/\text{s}$]

Both line width and line height decrease with increasing scanning speed. The product of height and width is used as a measure of the line's cross-sectional area, which is shown in figure 2.9

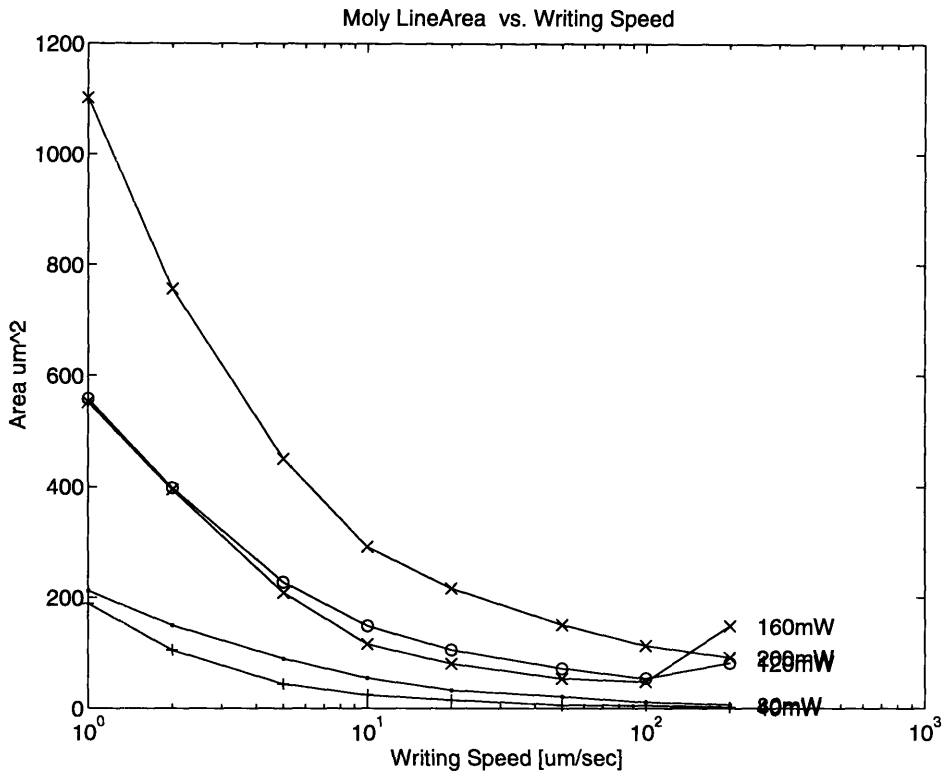


Figure 2.9 : Molybdenum line cross-section [μm^2] as a function of writing speed [$\mu m/s$] using a CW Argon Laser.

As expected, the cross section decreases with speed. The resistivity can be calculated by combining the area obtained with the resistance from figure 2.9. The resistivity is shown in figure 2.10

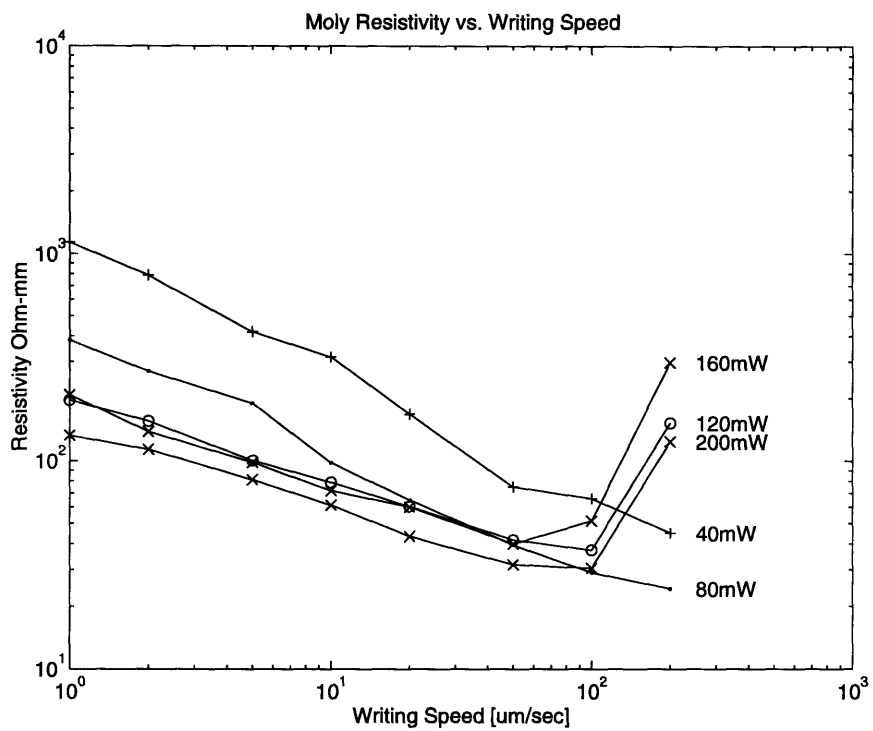


Figure 2.10 : Molybdenum line resistivity [Ω -mm] as a function of writing speed [$\mu\text{m/s}$] using a CW Argon Laser.

The calculation indicates that the material resistivity decreases as the scanning speed increases, except for speeds of $2000 \mu\text{m}$, where the resistivity increases. Also, resistivity is a decreasing function of laser power.

2.2 Platinum

Figure 2.11 shows the resistance of laser-deposited platinum lines as a function of writing speed and laser power. The CW Argon laser was pumped at powers ranging from 40mW up to 200 mW, while the XY stage was scanned from $1 \mu\text{m}/\text{s}$ up to 2000 $\mu\text{m}/\text{s}$.

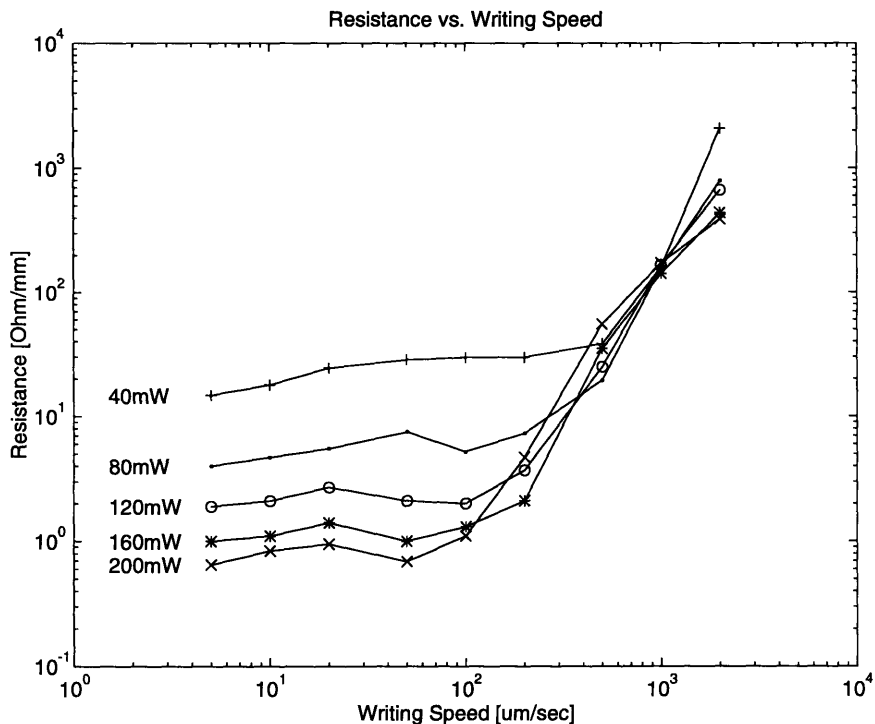
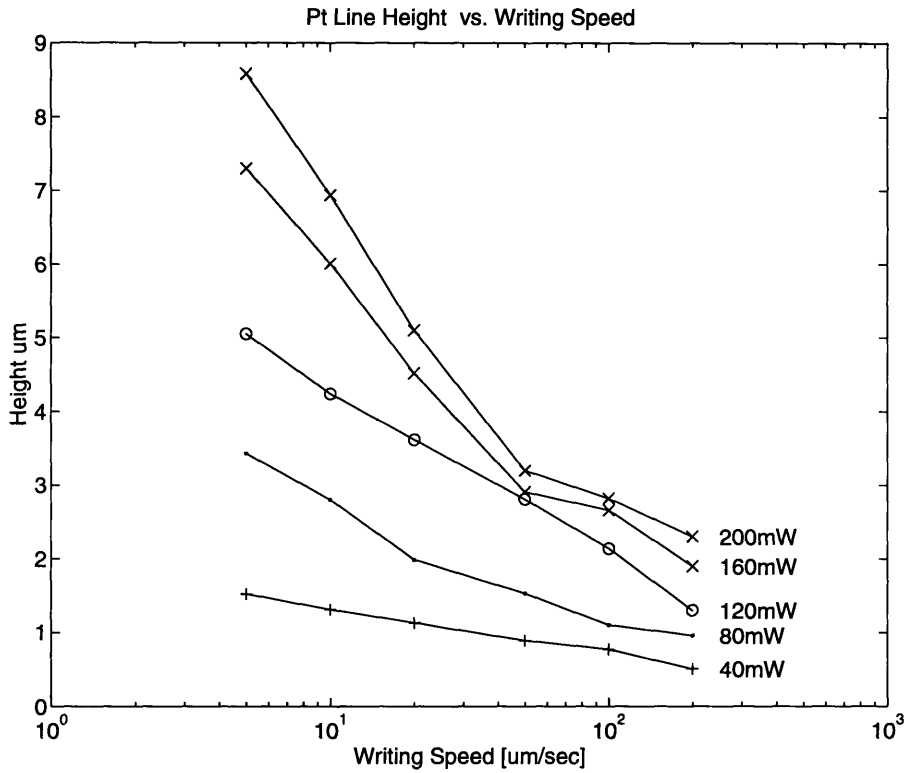


Figure 2.11 : Platinum line resistance [Ω / mm] as a function of writing speed [$\mu\text{m}/\text{s}$] using a CW Argon Laser.

Line resistance increases for increasing scanning speeds, as it did for the molybdenum deposit. There does not appear to be a clearly defined “saturation” speed, as the one observed in the case of Copper and Gold. Again, resistance decreases as laser power increases. The variation of line height with scanning speed is shown in figure 2.12.



*Figure 2.12 : Platinum line height [μm] as a function of writing speed [$\mu\text{m/s}$]
using a CW Argon Laser.*

The measured height decreases as scanning speed increases with constant laser power.
Increasing power for constant speed results in increased height.

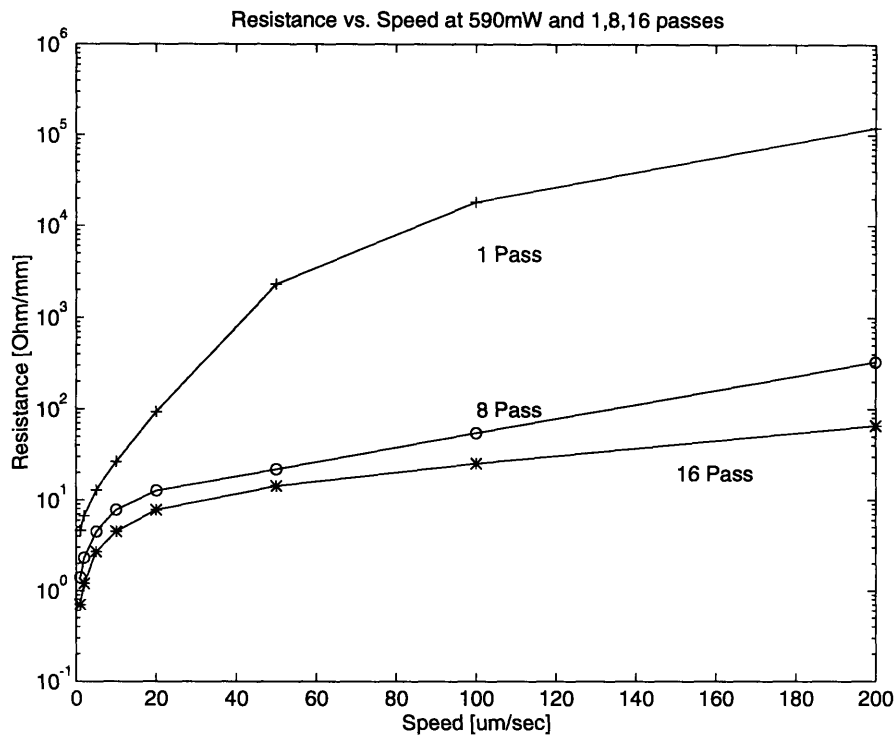


Figure 2.13 : Platinum line resistance [Ω /mm] as a function of writing speed [$\mu\text{m}/\text{s}$] and number of passes using a pulsed, frequency doubled Nd:YLF laser.

Line resistance decreases if multiple passes are performed, as can be seen from figure 2.13. Resistance increases for increasing speed, but decreases with increasing number of passes.

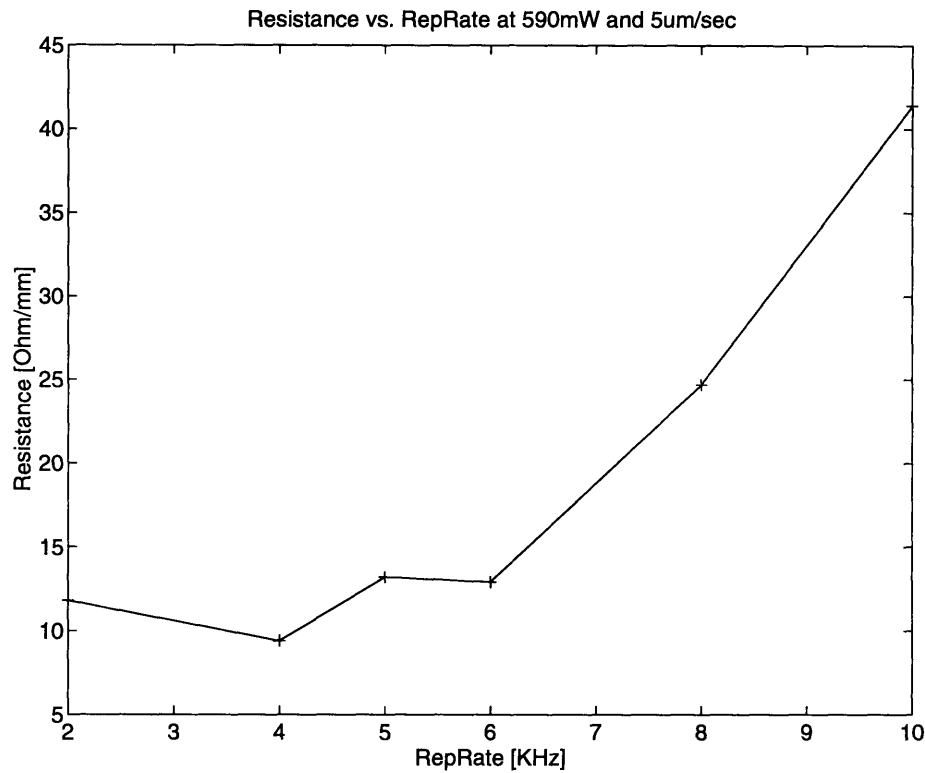


Figure 2.14 : Platinum line resistance [Ω /mm] as a function of rep rate [KHz] at constant speed using a pulsed, frequency doubled Nd:YLF laser.

Increasing rep rate increases the line resistance, for constant laser power and scanning velocity (Figure 2.14)

2.3 Discussion

The phenomena observed during the LCVD process are the result of a coupling between laser power input (modulated by substrate and deposit absorvity) and heat dissipation (through the substrate and the deposited thin film conductor). Figure 2.15 illustrates the relevant geometry.

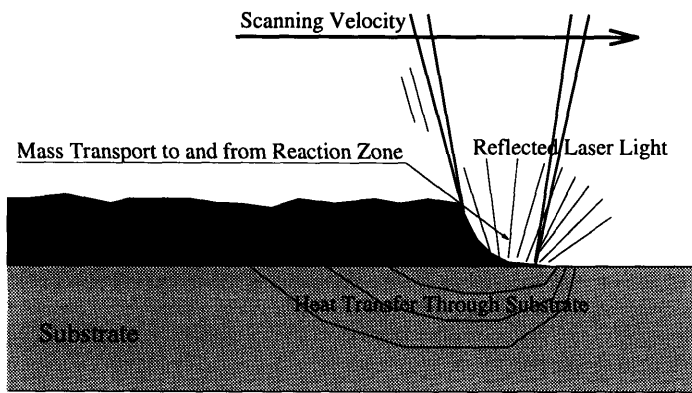


Figure 2.15 : Factors affecting the laser-assisted CVD process

There are several sequential chemical reactions involved in the decomposition and/or combination of the precursor compounds before the final product nucleates on the substrate surface. The various stages may be activated by the laser light itself or by the thermal reactions caused by the laser.

To complicate this, the temperature field and the concentration of reactants and products in the microreaction zone is influenced by:

- Heat input from the laser, and the way this is modulated because of variations in reflectivity that take place as the substrate is being covered with deposit.
- Heat transfer through the substrate and the deposit. The spatial extent to which there is a significant temperature rise is an important determinant of the linewidth, an important resolution-limiting factor.
- Mass transport of reactants and products to and from the microreaction zone.

These factors are all affected by the laser power, the scanning speed and the laser rep rate (in the pulsed case).

Despite the complexity of the process, some salient aspects of the data in sections 2.1 and 2.2 can be explained by a simple balance of the thermal coupling in the reaction zone. Factors that increase the temperature should increase the amount of deposited material, and factors that decrease temperature should decrease the deposited mass.

The simplest intuitive expectations are that as the laser power increases more deposit should be observed, and that increasing scanning velocity should result in less deposit, since heat input per unit mass of substrate decreases with increasing speed.

The results only partially match these expectations. Figure 2.16 shows a typical experiment during which all parameters are kept constant, except speed that decreases from left to right, going from $2000 \mu\text{m/s}$ to $5 \mu\text{m/s}$.

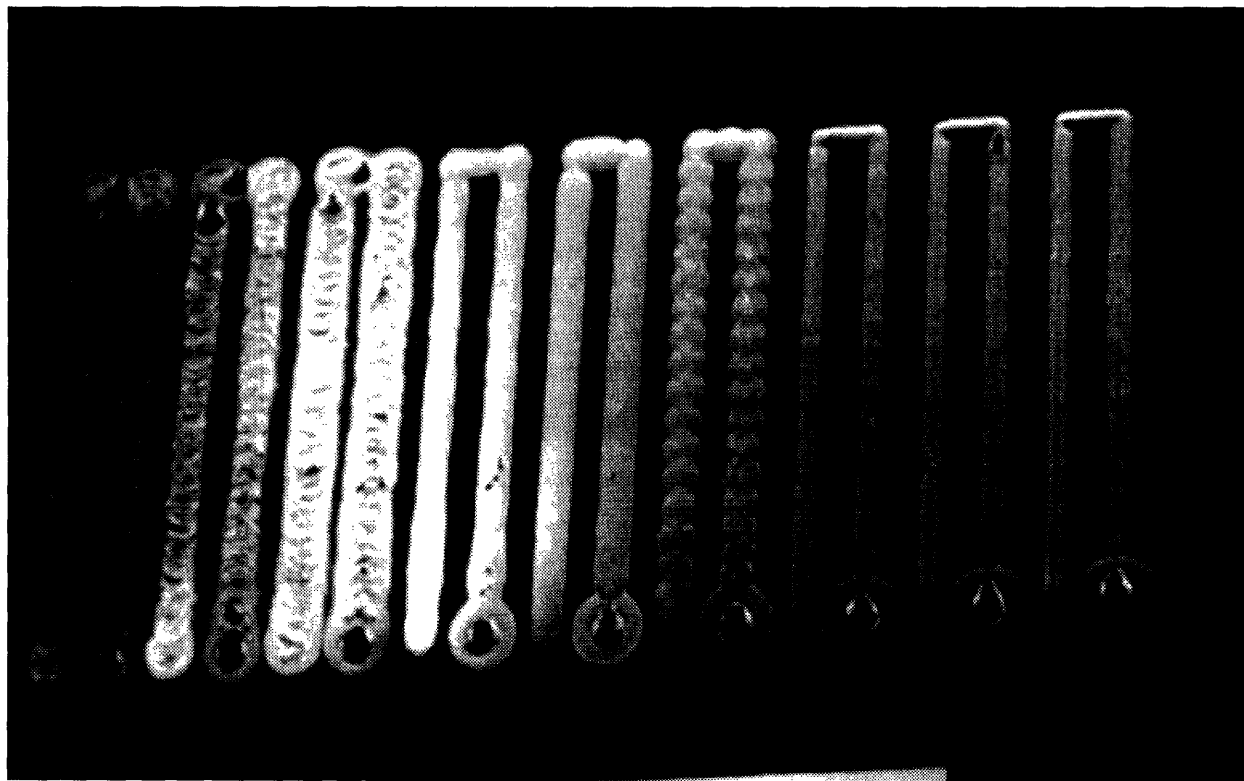


Figure 2.16 : Platinum lines deposited at constant power and speeds ranging from $2000 \mu\text{m/s}$ (left) to $5 \mu\text{m/s}$ (right)
Speeds (left to right): $2000, 1000, 500, 200, 100, 50, 20, 10, 5 \mu\text{m/s}$

A number of observations can be made about the SEM shown in figure 2.16:

- A periodic deposit structure is observed at a scanning speed of $50 \mu\text{m}/\text{s}$.
- The line to the right of the periodic structure (written at $20 \mu\text{m}/\text{s}$) is *thinner* than the line to the left of it, which was written at $100 \mu\text{m}/\text{s}$.
- substrate damage is only observed for the highest ($1000 \mu\text{m}/\text{s}$ and $2000 \mu\text{m}/\text{s}$) speeds.

All these points contradict the expected trends and must be explained.

The periodic structure itself has been observed by a number of researchers. A number of explanations have been put forth, but as far as the author is aware, no verifiable model exists that correctly predicts a speed-dependent periodic instability.

The fact that the deposited line is *thin* for speeds below $50 \mu\text{m}/\text{s}$ and *thick* at speeds above that does not conform with the expectation of thinner lines for decreasing energy input per unit mass. The energy input per unit mass decreases for increasing speed, and the line still becomes wider, signalling wider thermal diffusion. This “inverted” relationship between deposited mass and scanning speed can also be seen from the experimental data for platinum and molybdenum.

In a similar fashion, it is counterintuitive that substrate damage occurs only at high scanning speeds, when for the same power but lower speed no damage is discernible. One would expect the amount of damage to be proportional to the energy absorbed by the substrate, which is high for slow scanning speeds and low for high scanning speeds.

A more detailed understanding of the deposition process is needed in order to understand the results. The model that was developed to explains these irregularities as a result of an abrupt change in surface reflectivity caused by the deposition. The reasoning that leads to such an explanation of the results is presented in chapter 4.

Chapter 3

Applications

3.1 A typical modification sequence

The first step in any repair will be to locate the operation site on the chip. This usually entails some amount of navigation depending on chip complexity. Figure 3.1(left) shows the chip as it is seen through the low magnification objective. The crosshair is located on a transistor that will be modified.

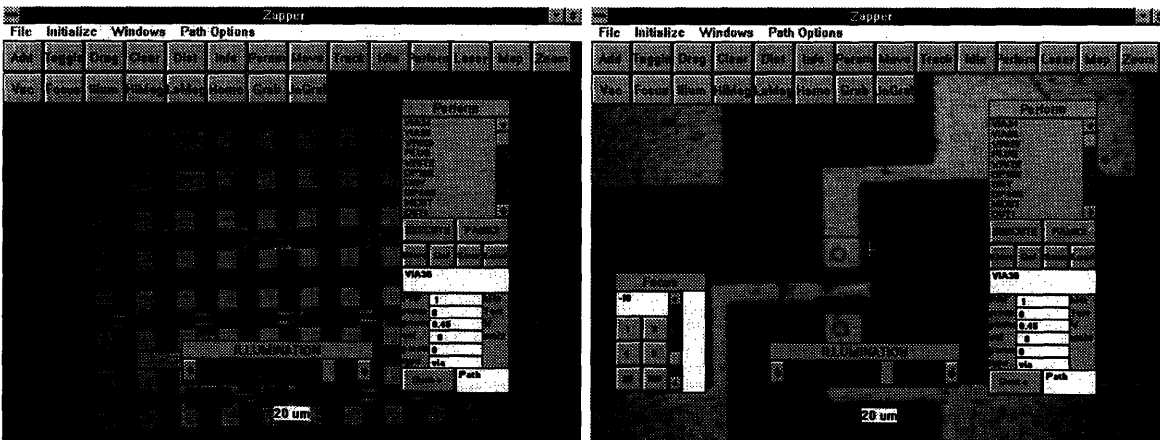


*Figure 3.1 : The site is located at low magnification
and the high magnification objective is then selected*

Figure 3.1(right) shows the same transistor using the high magnification objective. The transition to high magnification is achieved using . The next step is to select a set of process parameters for the cut operation. In this example, the parameter set

stored under the name WRITE was selected. These parameters select a 10KHz pulse rate, at a pump power of 0.99 W for the laser. The speed is set at 10 um/s and only one pass is specified. A short path across the conductor that will be severed is defined using **EXECUTE** twice.

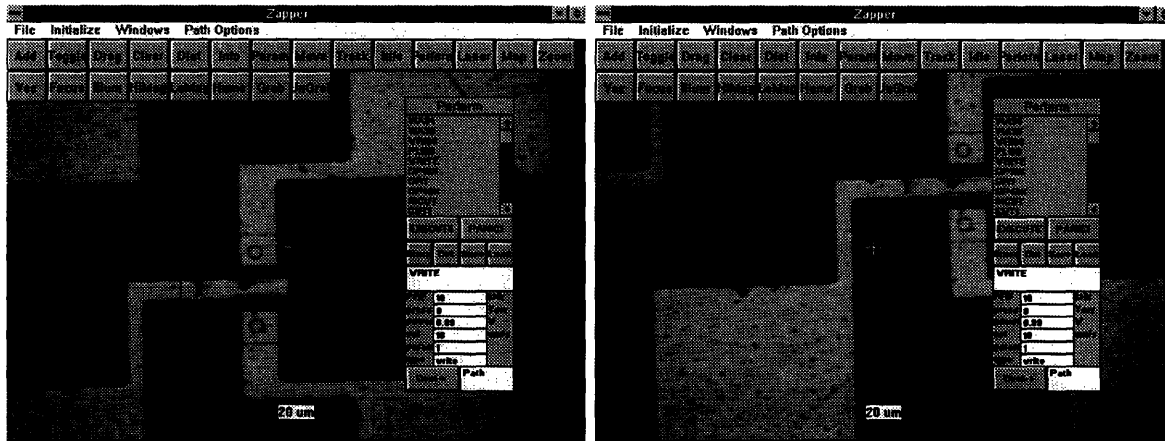


Figure 3.2 : The path is created, and the operation is performed

Using **EXECUTE** causes the operation to be performed. Note that the substrate is affected by the laser but not the conductor. The operation was not successful. This can happen from time to time if the process parameters are not properly set. (Figure 3.2)

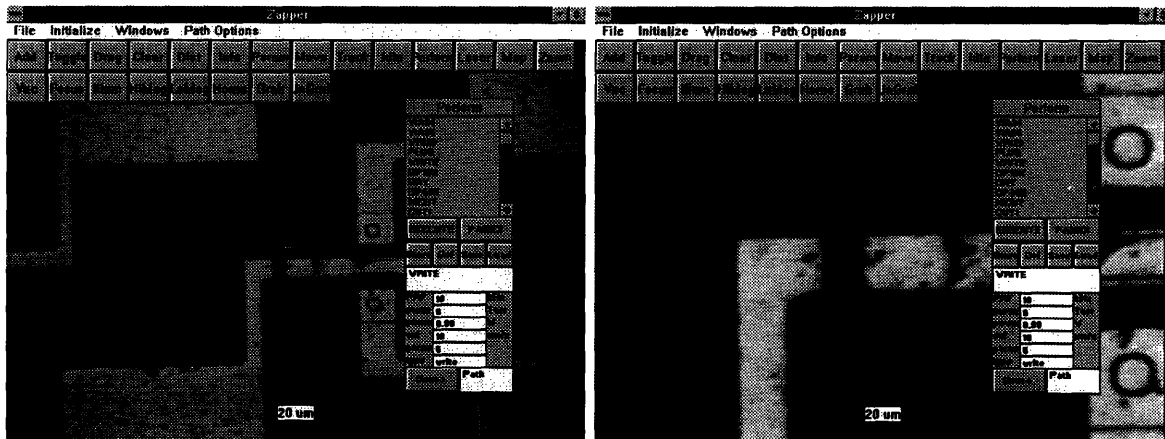


Figure 3.3 : The operation is repeated until a good cut is obtained.

To correct this, a higher number of repetition is set (5) and the process is repeated. This time, the operation is successful, as can be seen from the zoomed-in view at

figure 3.3(right)

3.2 A Severed Wire is Reconnected

More complicated structures can be created using the right combination of via and path operations.

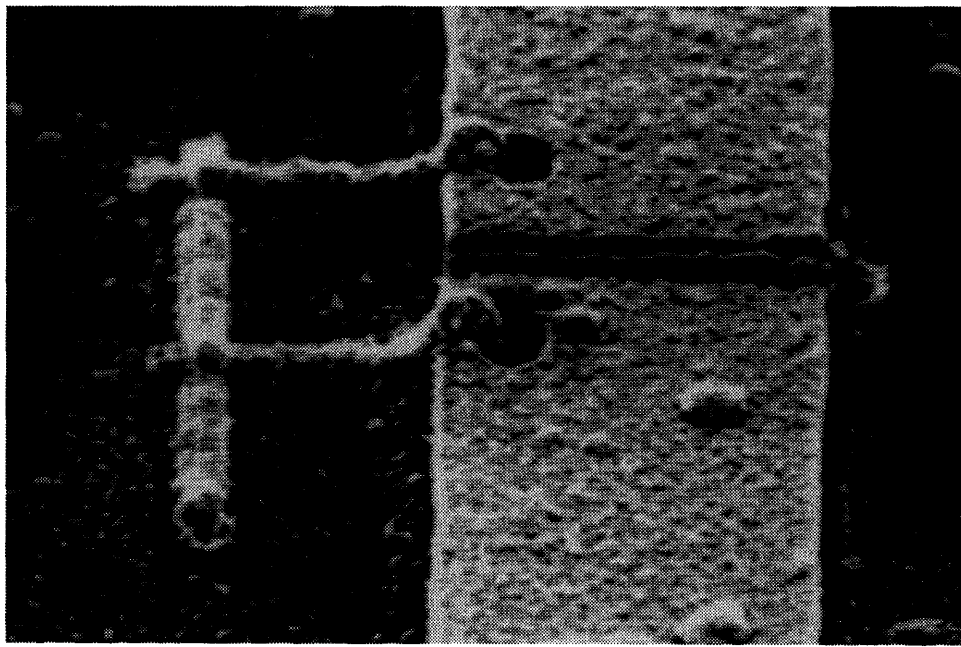


Figure 3.4: A reconnected wire

This example shows all the operations that can be performed using the LCVD system:

- The copper wire (width about 10 um) was severed using the laser under vacuum
- two via holes were drilled through the passivation layer on top of the wire
- the via holes were filled with deposited platinum (plugs)
- the plugs were connected together with a deposited wire, thus re-connecting the severed path

The use of via holes at the endpoints of the deposited platinum wires makes it possible to write over a layer of passivation without electrical contact to the conductors under the passivation. This is especially important when operating on densely populated regions of a chip.

3.3 A Staircase Via

Another example of a more involved operation possible with the software is a staircase via dug into ployimid to reach a buried copper wire connecting elements of a multichip module (MCM). Because the via is about 50 um deep, it is not possible to write a line from the exposed wire to the surface of the Polyimide. In order to accomplish this, a “staircase” of 5um stairs is constructed and the line is made to “descend” over it.

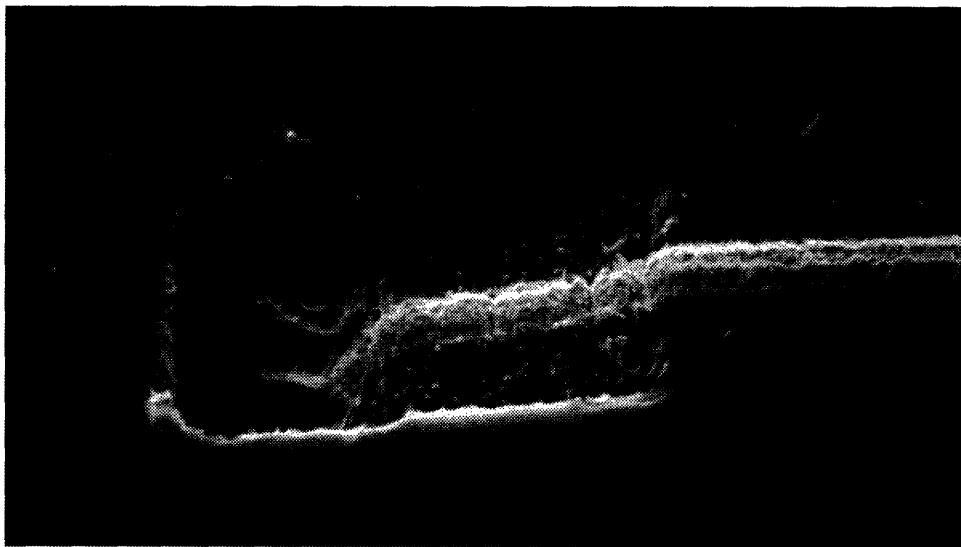


Figure 3.5: A Staircase via

The staircase is constructed by superimposing multiple raster scans with successively lower focal points. The path needed to do this is constructed automatically using the **Staircase** macro.

3.4 Low-resistance platinum-to-copper contacts

Contact resistance must be kept as low as possible for optimal rewiring results. Figure 3.6 demonstrates very low contact resistance platinum lines attached to a thick copper conductor.

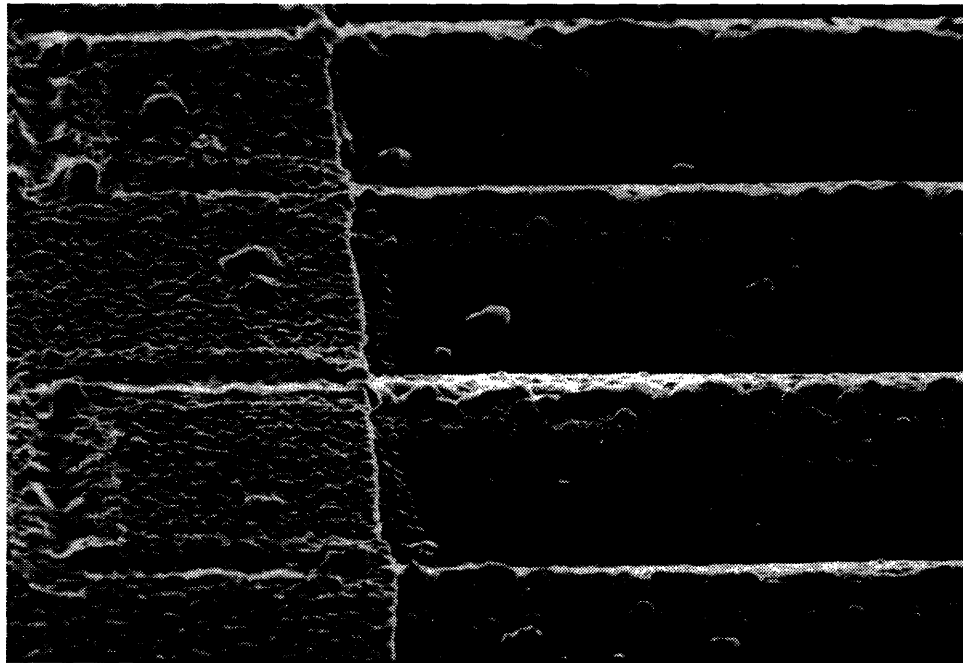


Figure 3.6: Low-resistance contact between
deposited platinum and copper conductor

The low resistance value is achieved by melting the deposit on top of the copper. The resulting contacts are of excellent quality.

3.5 Depassivation

In some rework cases, the passivation layer covering the chip needs to be removed before the actual repair can be attempted. A technique similar to the one used to make the “staircase via” can be used to remove a $1\text{-}\mu\text{m}$ layer of passivation.

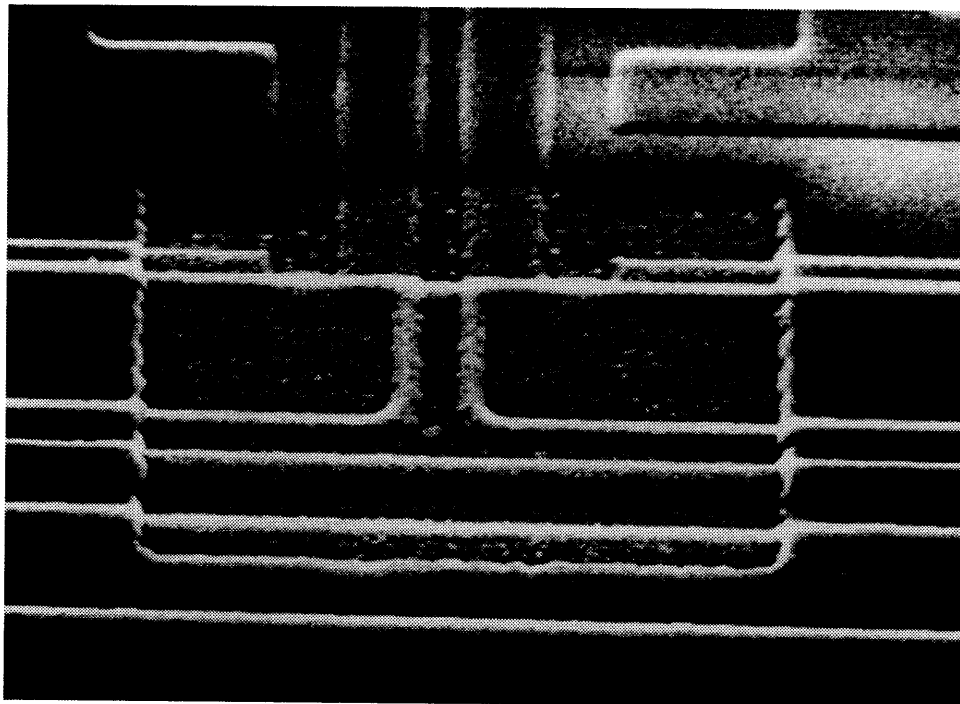


Figure 3.7: A 30-by-50 μm depassivated window.

If the process parameters are chosen properly, there is no damage to the uncovered microelectronics.

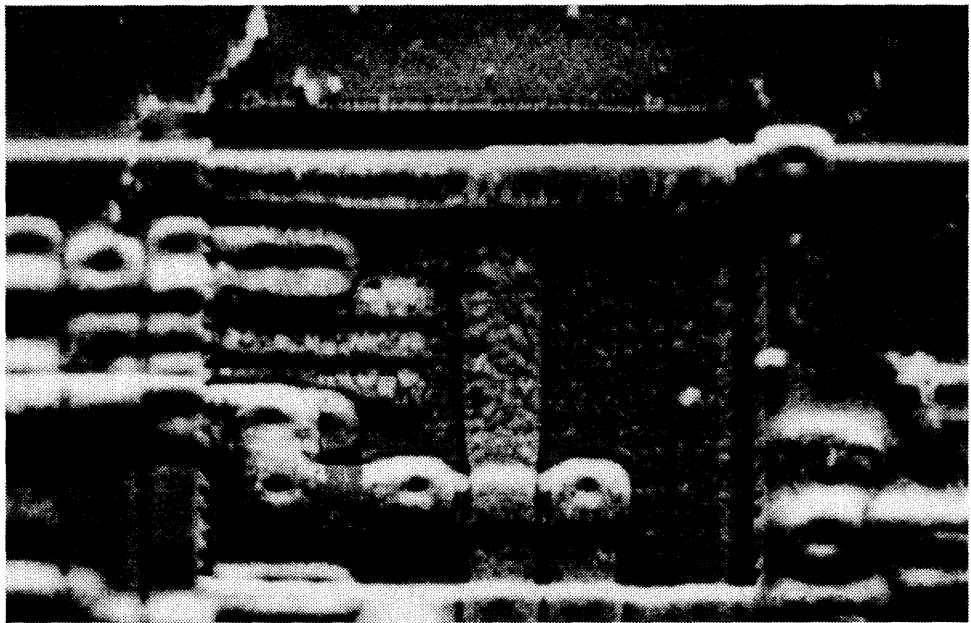


Figure 3.8: A 30-by-20 μm depassivated window, undamaged electronics

Chapter 4

Modeling

Laser-drive pyrolytic CVD was studied using both analytical and numerical models. The deposition process is determined by heat transport, mass transport and chemical kinetics considerations. A detailed treatment has to take into account all these aspects of the problem, a task which has not yet been sufficiently addressed in its entirety. Most of the sub-problems, however, have been treated previously.

Heat diffusion from a source which is scanned at a constant velocity has been calculated analytically by Lax¹, Cline², Moody³ and others^{4 5 6}. The non-linear cases can be addressed either analytically using a Circhoff transform or numerically.

The mass transport aspect is treated by Jensen⁷ and others. The kinetics are highly complex and vary for each combination of precursor, substrate and excitation mechanism and are therefore treated in a case-by-case basis. The main distinction is between Photolyticaly as opposed to Pyrolyicaly activated deposition and single as opposed to multi-composition precursor.

In light of the considerable complexity of the physical problem, numerous simplifications have to be made. The purpose of this investigation was to obtain some insight

¹ M.Lax, *J. Appl. Phys.* **48**, 3819 (1977)

² H.E. Cline and T.R. Anthony, *J. Appl. Phys.* **48**, 3895 (1977)

³ J.E. Moody and R.H. Hendel, *J. Appl. Phys.* **53**, 4364 (1982)

⁴ A. Kar, M.N. Azer and J. Mazumder, *J. Appl. Phys.* **69**, 757 (1991)

⁵ R.J. Harrash *J. Appl. Phys.* **48**, 2370 (1977)

⁶ S.D. Allen, *J. Appl. Phys.* **52**, 6501 (1981)

⁷ D.C. Scouby and K.F. Jensen, *J. Appl. Phys.* **63**, 198 (1988)

of the mechanisms that affect the morphology of platinum deposits on polyamid and silicon substrates, and specifically the factors that limit the achievable spatial resolution.

A numerical scheme for the solution of the coupled heat diffusion - deposition problem was developed, and a number of numerical experiments were performed. Results were compared to experimentally observed structures and a number of features were found to be predicted by the simple model developed.

4.1 Analytical Solutions

Analytical solutions to the heat diffusion problem are limited to very simple cases. They are, however, very valuable because the insight gained from an analytical approach invariably leads to a better understanding of the more complex problems. The results obtained are used to provide initial guesses or bounds for the numerical model. They are useful to verify results, which can sometimes be erroneous because of numerical instability, roundoff errors or simple programming bugs.

Three techniques have been used in the literature to obtain such solutions:

- Direct integration. This only works for extremely simple cases. The solutions obtained this way are used as building blocks to approach more difficult problems
- Series expansion and separation of variables. The procedure involves the expansion of the solution into a series of eigenfunctions particular to the coordinate system used (sine and cosine for cartesian, bessel for cylindrical or legendre for spherical) and use of the boundary conditions to determine values for the coefficients ⁸.
- The Green's Function technique entails the expression of boundary and initial conditions as a superposition of Greens Functions, which allows the temperature field to be calculated as a superposition of known, simple analytic solutions ⁹. This is a very powerful method which can treat unusually complex cases. It is also very suitable for incorporation into numerical schemes.

The most appropriate approach for the case of a moving gaussian beam irradiating a semi-infinite body is the Green's function technique, which leads to an (almost) closed form solution for the linear case. The non-linear case for variable thermal conductivity can be transformed into an equivalent linear problem using the Kirchhof transform, which allows the calculation of a “linear temperature” which can then be transformed back into a real, “nonlinear temperature” using the inverse transform.

4.2 Green's Function derivation

The most fundamental heat problem is the diffusion of a heat amount of q_0 that suddenly appears at $x = 0$ and $t = 0$. The equations for this case are:

⁸ H.S. Carslaw and J.C. Jaeger, *Conduction of Heat in Solids* (Oxford U.P., New York, 1959)

⁹ J. Hill and J.N. Dewynne, *Heat Conduction*. (Blackwell Scientific Publications, 1987)

$$\frac{\partial T}{\partial t} = \alpha \frac{\partial^2 T}{\partial x^2} \quad (4.1)$$

$$\lim_{x \rightarrow \infty} T = 0 \quad (4.2)$$

$$T(x, 0) = q_0 \delta(x) \quad (4.3)$$

Since (1) is invariant under the stretching transformation,

$$x^* = \lambda x \quad (4.4)$$

$$t^* = \lambda^2 t \quad (4.5)$$

$$T^* = T/\lambda \quad (4.6)$$

Eliminating λ yields

$$x^*/\sqrt{t^*} = x/\sqrt{t} \quad (4.7)$$

$$T^*\sqrt{t^*} = T\sqrt{t} \quad (4.8)$$

Because $T(x, t)\sqrt{t}$ is a non-dimensional quantity, it is possible to formulate a function $\Psi(x/\sqrt{t})$ such that:

$$T(x, t)\sqrt{t} = \Psi\left(\frac{x}{\sqrt{t}}\right)$$

and hence:

$$T(x, t) = \frac{1}{\sqrt{t}} \Psi\left(\frac{x}{\sqrt{t}}\right)$$

has to be the functional form of the solution. Substituting $\zeta = x/\sqrt{t}$ yields an ordinary linear differential equation:

$$2\alpha \ddot{\Psi} + \zeta \dot{\Psi} + \Psi = 0$$

where differentiation with respect to ζ is denoted by dotted variables. The solution is:

$$T(x, t) = q_0 \frac{e^{-\frac{x^2}{4\alpha t}}}{2\sqrt{\pi\alpha t}}$$

2D and 3D solutions are found using the superposition principle:

$$T(x, y, z) = T(x)T(y)T(z)$$

The 3D solution is:

$$T(x, y, z, t) = q_0 \frac{e^{-(x^2+y^2+z^2)/(4\alpha t)}}{8(\pi\alpha t)^{3/2}}$$

The 3D solution for $q_0 = 1$ will be denoted as $G(x, y, z, t, x^*, y^*, z^*, t^*)$, and therefore $T(x, y, z, t) = q_0 G(x, y, z, t, x^*, y^*, z^*, t^*)$, where (x, y, z, t) is any location in space-time and (x^*, y^*, z^*, t^*) is the location of the instantaneous heat.

Continuous, non-instantaneous distributions of heat can be viewed as a superposition of instantaneous, point sources. To do this a well known identity for the δ function is used:

$$f(x_0) = \int_{-\infty}^{+\infty} f(x)\delta(x_0 - x)dx \quad (4.9)$$

Using $Q()$ for $f()$, extending this to four dimensions and writing x, y, z instead of x_0, y_0, z_0 and x^*, y^*, z^* instead of x, y, z , we get the desired superposition:

$$Q(x, y, z, t) = \int_{-\infty}^t \int_{-\infty}^{+\infty} \int_{-\infty}^{+\infty} \int_{-\infty}^{+\infty} Q(x^*, y^*, z^*, t^*)\delta(x-x^*, y-y^*, z-z^*, t-t^*)dz^*dy^*dx^*dt^* \quad (4.10)$$

The temperature distribution caused by the point source $q(x, y, z, t) = Q(x, y, z, t)\delta(x-x^*, y-y^*, z-z^*, t-t^*)$ is known, and equal to $Q(x^*, y^*, z^*, t^*)G(x, y, z, t, x^*, y^*, z^*, t^*)$, where (x^*, y^*, z^*, t^*) is the location of the source and (x, y, z, t) is any point in space-time. The temperature because of all sources is the superposition of the temperatures because of each one of them:

$$T(x, y, z, t) = \int_{-\infty}^t \int_{-\infty}^{+\infty} \int_{-\infty}^{+\infty} \int_{-\infty}^{+\infty} Q(x^*, y^*, z^*, t^*) G(x, y, z, t, x^*, y^*, z^*, t^*) dz^* dy^* dx^* dt^* \quad (4.11)$$

The heat caused by moving gaussian laser beam is:

$$Q(x, y, z, t) = P\delta(z) \frac{e^{-[(x-vt)^2+y^2]/2R^2}}{2\pi R^2} \quad (4.12)$$

The semi-infinite G differs from the infinite one by a factor of two:

$$G_{semi-infinite} = \frac{\exp\left[-\frac{r^2}{4D(t-t)}\right]}{4[2\pi R(t-t)]^{\frac{3}{2}}} = 2G_{infinite} \quad (4.13)$$

Where $r^2 = (x - x^*)^2 + (y - y^*)^2 + (z - z^*)^2$ and the surface is at $z = 0$. The factor-of-two change is the result of half the material being subjected to an unchanging heat input.

Substituting the expression for the moving, gaussian laser beam along with the Green function for the semi-infinite space into the temperature field expression just arrived at, we get an integral that yields the time-dependent temperature field caused by a scanning gaussian laser beam. The good thing about this is that all the spatial integrations (i.e. from $-\infty$ to $+\infty$ over x , y and z) can be expressed as closed-form limits. This only leaves the integration over time ¹⁰:

$$T(x, y, z, t) = \frac{Q}{C_P} \int_{-\infty}^t \frac{\exp\left[-\left(\frac{(x+ut^*)^2+y^2}{2R^2+4Dt^*} + \frac{z^2}{4Dt^*}\right)\right]}{\sqrt{\pi^3 Dt^* (2R^2 + 4Dt^*)}} dt^* \quad (4.14)$$

The resulting temperature distribution can be interpreted as a superposition of time-exponentially decaying gaussians that originate at ut , the moving laser spot center, as can be seen from figure 4.1

¹⁰ H.E. Cline and T.R. Anthony, *J. Appl. Phys.* **48**, 3895 (1977)

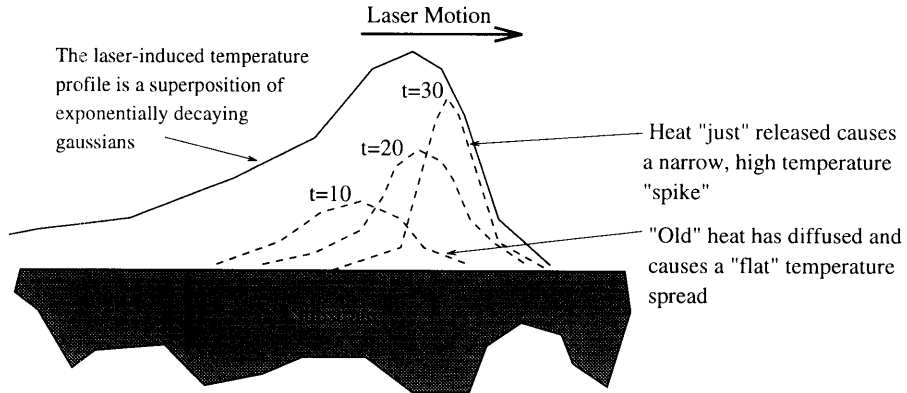


Figure 4.1 : Laser-induced temperature profile

The steps required to arrive at the solution were:

- Solve the 1D diffusion of an instantaneous heat quantity.
- Generalize the solution for 2D and 3D because of linearity.
- Formulate semi-infinite space solution from 3D solution using a symmetry argument.
- Obtain solution for non-instantaneous heat sources by means of superposition.
- Formulate special case for moving gaussian heat source.

The resulting integral does not have a closed form, but it can be easily evaluated numerically using any of a number of well known techniques. Performing the integration for each of a grid of points on the substrate we get the surface temperature distribution:

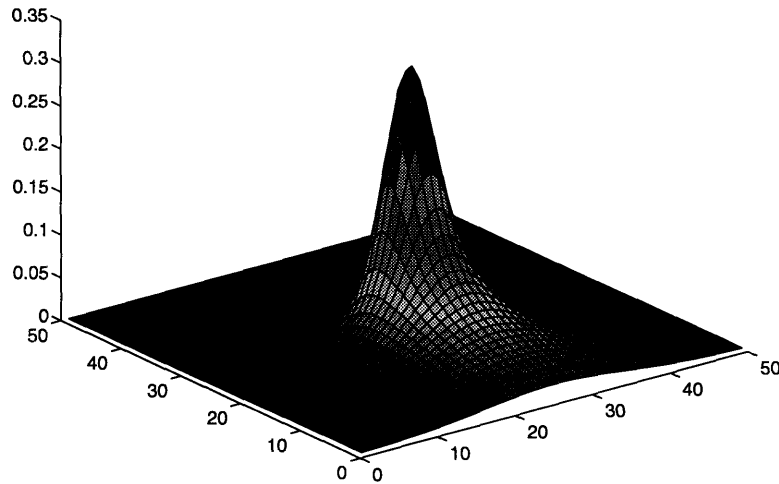


Figure 4.2 : Surface temperature from scanned gaussian laser

A listing of the code used to perform the integration follows:

```
main(int argc, char **argv)
{
    double t1,t2,t3,t4;
    int i,j,k;
    double x,y,r;
    for(i=0;i<IMAX;i++){
        for(j=0;j<JMAX;j++){
            x=20*(i*1.0-(double)(IMAX)*0.5);
            y=20*(j*1.0-(double)(JMAX)*0.5);
            r=sqrt(x*x+y*y);
            if(r<0.01)r=0.01;
            t=0.1;
            for(k=0;k<MaxN;k++){
                t1=P*exp(-((x+V*t)*(x+V*t)+y*y)/(2*R*R+4*D*t))/C;
                t2=sqrt(Pi*Pi*Pi*D*t)*(2*R*R+4*D*t);
                T[i][j]+=dt*t1/t2;
                t+=dt;
            }
            printf("%lf ",T[i][j]);
        }
        printf("\n");
    }
}
```

The time-evolution of the temperature along the centerline of the axis of motion can be seen in the next figure. The laser is switched on at $t=0$ and the figures correspond

to the temperature profiles at times $t = \Delta t$, $t = 10\Delta t$, $t = 50\Delta t$ and $t = 99\Delta t$. Note that after some time the temperature profile reaches the steady-state shape shown in figure 4.3

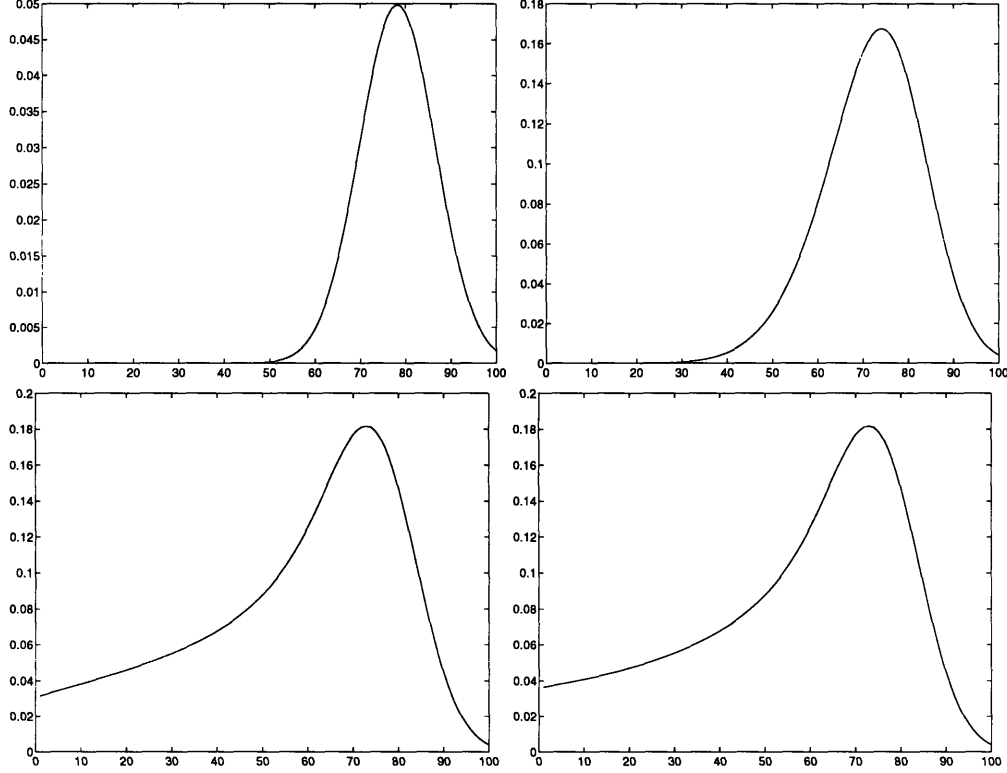


Figure 4.3 : Time evolution of centerline temperature after switch-on

The solution presented here assumes constant thermal capacities and thermal conductivities. This is the *linear* case.

Non linear problems are much harder to solve and do not usually have analytical solutions. The temperature-dependent conductivity case can be treated by using the Kirchoff transform ¹¹, a change of variable which eliminates this particular non-linearity. The substitution used is

$$\Theta(T) = \int_{T_0}^T \frac{K(T)}{K_0} dT$$

It can be easily verified that the the non-linear temperature dependence of the thermal conductivity is removed, resulting in an equivalent linear problem that can be solved

¹¹ M.Lax, *Appl. Phys. Lett.* **33**, 786 (1978)

with any method, including the Green's function approach presented previously.

4.3 Numerical Solutions

The heat diffusion problem is amenable to a large number of numerical solution procedures. These can be roughly classified as follows:

- Finite Difference and Finite Volume
- Finite Element
- Boundary Element
- Monte Carlo

Finite Element solutions have historically been widely used, because early interest in numerical results arose from the need to obtain a solution for the coupled heat diffusion and material strain problem, during the calculation of structural thermal stresses. Since structural problems are very well suited to FEM treatment, the same technique was also employed for the thermal calculation. Scouby and Jensen have used the FEM method to investigate laser-assisted pyrolytic deposition with coupled mass transport ¹².

Finite difference methods have traditionally been very popular for computational fluid dynamics (CFD) applications, and are significantly simpler to implement than FEM. The boundary element method is a more recent approach that uses an integral transform technique to express the solution in terms of the boundary conditions in a very economical way. It basically is the numerical counterpart of the Green's function technique. It is very efficient because much of the solution's structure is already present in the initial formulation. Arnold and Bauerle have used this method to simulate the growth of tungsten in pyrolytic laser CVD. ¹³

¹² D.C. Scouby and K.F. Jensen, *J. Appl. Phys.* **63**, 198 (1988)

¹³ N. Arnold and D. Bauerle, *Microelectronic Engineering* **20**, 43-54 (1993)

The Monte-Carlo method differs radically from the other three in that it does not directly start from the heat diffusion equation or a discrete algebraic approximation. Solution values at specific points are instead calculated using a random-walk technique which mirrors the physical process underlying the diffusion phenomenon. The temperature so calculated converges to the true solution if a large enough number of “walks” is undertaken. Unfortunately, the fundamental rate of convergence is inversely proportional to the square of the iterations, therefore making this a very time consuming procedure. A noteworthy property of the Monte-Carlo approach is its unconditional stability and the ease with which it can be used to treat even the most complex cases.

4.4 A finite difference scheme for the 3D unsteady case

The essence of the finite difference method is the substitution of partial derivatives with finite differences, which are used as approximations of the exact derivatives. In the process of doing so the differential equation is transformed into an algebraic relationship between neighboring nodes of the solution domain. The original equation is recovered in the limit of an infinitely fine discretization. The set of algebraic equations for all nodes of the domain, along with the boundary conditions, forms a system of simultaneous equations which can be solved using any of a number of suitable techniques.

The heat diffusion equation under consideration is the linear, 3D, unsteady form, and the independent variables are therefore three spatial coordinates and time.

Since this is an unsteady problem, the solution procedure will repeatedly calculate the temperature distribution at $t + \Delta t$ as a function of the distribution at t . This procedure is called *time-marching*

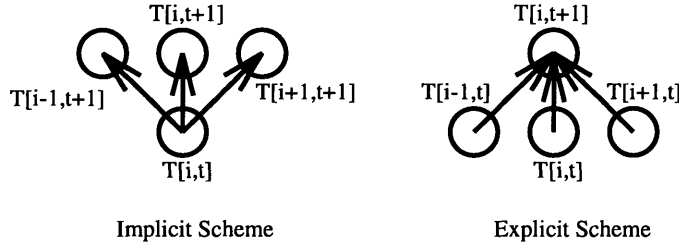


Figure 4.4 : Implicit vs. Explicit

Depending on the form of the functional dependence, the time-marching is either *explicit* or *implicit*. In the *explicit* formulation, it is possible to calculate each future temperature value as a function of the present temperature at neighboring nodes **only**. In the *implicit* case, future temperature values are functions not only of present but also of neighboring future values. This means that the whole future temperature distribution has to be calculated at once, as a solution to a set of simultaneous equations.

A Central Space, Forward Time (CSFT) discretization was used, which means that the $i - 1$ and $i + 1$ indices can be exchanged without changing the formula, but not so for the n and $n + 1$ index. This reflects the fact that the underlying differential equation is parabolic in time and elliptic in space.

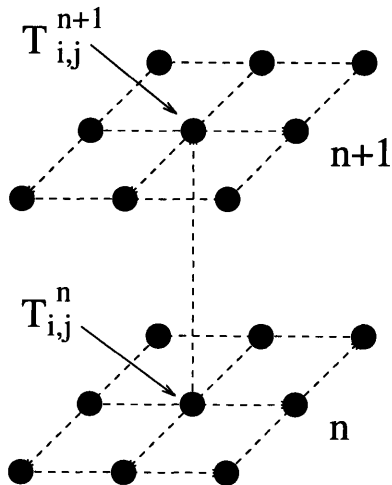


Figure 4.5 : 2D unsteady heat diffusion computational node, with neighbors

The 3D diffusion equation that will be solved numerically is:

$$\frac{\partial T}{\partial t} = \alpha \left[\frac{\partial^2 T}{\partial x^2} + \frac{\partial^2 T}{\partial y^2} + \frac{\partial^2 T}{\partial z^2} \right]$$

The functional form of the time-marching scheme arrived at depends on the choice of discretization. There is no freedom to choose nodes for the time derivative:

$$\frac{\partial T}{\partial t} = \frac{T_{i,j}^{n+1} - T_{i,j}^n}{t^{n+1} - t^n}$$

The nodes chosen to express the spatial derivatives can be either be in the present (i.e. n index) or in the future (i.e. $n + 1$) since in both cases we obtain an equally valid approximation to the spatial derivative.

Choosing present (i.e. n) values gives:

$$\begin{aligned}\frac{\partial^2 T}{\partial x^2} &= \frac{T_{i+1,j}^n + T_{i-1,j}^n - 2T_{i,j}^n}{\Delta X^2} \\ \frac{\partial^2 T}{\partial y^2} &= \frac{T_{i,j+1}^n + T_{i,j-1}^n - 2T_{i,j}^n}{\Delta Y^2}\end{aligned}$$

This is an *explicit* discretization.

Choosing future (i.e. $n + 1$) values gives:

$$\begin{aligned}\frac{\partial^2 T}{\partial x^2} &= \frac{T_{i+1,j}^{n+1} + T_{i-1,j}^{n+1} - 2T_{i,j}^{n+1}}{\Delta X^2} \\ \frac{\partial^2 T}{\partial y^2} &= \frac{T_{i,j+1}^{n+1} + T_{i,j-1}^{n+1} - 2T_{i,j}^{n+1}}{\Delta Y^2}\end{aligned}$$

This is an *implicit* discretization.

Substituting these algebraic expressions into the heat diffusion equation, we get an algebraic relation between future, past and neighboring node temperatures, which can be solved numerically:

$$\frac{T_{i,j}^{n+1} - T_{i,j}^n}{t^n - t^{n-1}} = \alpha \left[\frac{T_{i+1,j}^n + T_{i-1,j}^n - 2T_{i,j}^n}{\Delta X^2} + \frac{T_{i,j+1}^n + T_{i,j-1}^n - 2T_{i,j}^n}{\Delta Y^2} \right]$$

solving for $T_{i,j}^{n+1}$ results in the equation that is used to implement an explicit time-marching solution procedure:

$$T_{i,j}^{n+1} = T_{i,j}^n + \alpha (t^{n+1} - t^n) \left[\frac{T_{i+1,j}^n + T_{i-1,j}^n - 2T_{i,j}^n}{\Delta X^2} + \frac{T_{i,j+1}^n + T_{i,j-1}^n - 2T_{i,j}^n}{\Delta Y^2} \right]$$

The fact that future values of temperature only appear once makes the equation solvable for $T_{i,j}^{n+1}$.

If the spatial derivatives were expressed in terms of furute values, i.e. $T_{i+1,j}^{n+1}$ and similar terms appeared in the equation, no explicit solution is possible. The resulting numerical scheme is *implicit* since the calculation of future values cannot be performed on a point-by-point basis. The future temperature distribution is obtained by solving the system of simultaneous equations for the future temperature values. This is usually done using some iterative procedure.

One of the simultaneous equations that enter the implicit calculation is:

$$T_{i,j}^{n+1} = T_{i,j}^n + \alpha (t^{n+1} - t^n) \left[\frac{T_{i+1,j}^{n+1} + T_{i-1,j}^{n+1} - 2T_{i,j}^{n+1}}{\Delta X^2} + \frac{T_{i,j+1}^{n+1} + T_{i,j-1}^{n+1} - 2T_{i,j}^{n+1}}{\Delta Y^2} \right]$$

The advantage of an explicit formulation is simplicity. The temperature value in the future only depends on the past temperature values of neighboring nodes, and the calculation can therefore be performed in one simple step. The disadvantage of the scheme is that it is only conditionally stable, i.e. the solution is only physically meaningful if certain restrictions on the discretization apply. The physical reason for these restrictions is that the calculation implies that neighboring nodes do indeed affect the node's future value within a time interval of ΔT . This limits the maximum time step for any given spatial discretization, and therefore the required computer time to reach a specific point in time.

The implicit formulation, on the other hand, is unconditionally stable, no matter how large the time step used. Because spatial dimensions are on the order of hundreds of μm , the maximum explicit time step allowed is on the order of microseconds. Since we are interested in timescales on the order of seconds, it follows that an explicit calculation will only yield the desired results after millions of iterations. A typical discretization has 50 by 50 by 50 nodes, and the advancement by one timestep into the future requires about 1 second on a typical workstation.

The conclusion of this line of reasoning is that an explicit scheme will require on the order of hundreds of hours of computer time to calculate the temperature distribution one second after the laser is turned on. The use of an implicit scheme is therefore unavoidable.

This scheme clearly lends itself to an iterative solution, whereby the equation just presented is repetitively applied to the future temperature field until further iterations produce no change.

The advancement by one time-step is therefore much more complicated than the equivalent explicit calculation. The use of a much larger time-step, however, by far outweighs the computational penalty imposed by the more complicated time-advancement procedure.

A number of refinements to the simple implicit method exist. Since the method can be made to advance time at any rate, by simply increasing the time-step, the main effort has been focused on increasing the accuracy of the solution that is obtained.

The most successful scheme is the Crank-Nickolson discretization, which substitutes the spatial derivatives with the mean value of the present and future discretization. This improves the accuracy of the scheme (as can be shown by considering the order of the Taylor-series terms that are neglected) and thus allows the use of an even larger time step for a given accuracy requirement.

4.5 Implementation of the 3D, unsteady heat diffusion solver

The physical dimensions of the slab were taken to be 100 by 100 um with a depth of 10 um.

The grid used was a 100 X 100 X 10 discretization, with uniform node spacing.

Because the interest was in physical understanding as opposed to accurate prediction, no adaptive meshing or other similar accuracy enhancing techniques were used.

The solution domain was represented as a 3D array of double-precision numbers:

```
/*
** Solution
*/
double T[IM][JM][KM][2];
double D[IM][JM];
char a[IM][JM][KM];
```

Two copies of the current solution values are needed in order to store the present and calculated future values at every time step. On the next step the previously future values are used as present one and the calculation results are stored in the previously present-value location. The fact that only the spatially-neighboring nodes are used for the calculation of the next value would allow for a more memory-efficient scheme to be used, one which would discard old temperature values after all future temperatures requiring them are calculated. At this point it seems that bottleneck preventing the calculation of finer grid meshes is computational speed and not available memory.

The zero-temperature-at-infinity boundary condition was used. This is a correct assumption only if the solution domain is large enough to make the amount of diffused heat reaching the boundary insignificant. For a smaller solution domain, the statement that the heat input at the laser spot will diffuse in an approximately spherically-symmetric manner at large distances from the laser spot is more appropriate.

For the current level of accuracy, a simple Diriclet-type boundary condition was used. Solution domain points are divided into the following types:

- **INTERIOR** All interior points contain no heat sources, and have no condition apart from the heat diffusion equation imposed upon them.
- **DIRICLET** These points have a constant temperature. They are not affected by the numerical algorithm, but their values affect the neighboring nodes.
- **NEUMANN** These are points on which a Neumann-type (specified heat flux) boundary condition is imposed. In fact, **NEUMANN** boundary conditions can be viewed as **DIRICLET** ones with a number of “imaginary” points attached to them, where the temperature of these “imaginary” points is given by some algebraic relationship derived from the required heat-flux.
- **SURFACE** These points have a heat-flux due to the laser associated with them.

The solution domain is organized as a cube filled with **INTERIOR** points, with all faces having a **DIRICLET** attribute, except for the ones on the $k=0$ face, which are of the **SURFACE** type. The initialization procedure that implements this works as follows:

```
{
    int i,j,k;
    for(i=0;i<IM;i++)for(j=0;j<JM;j++){
        D[i][j][0]=DZ/5.0;
        D[i][j][1]=DZ/5.0;
        for(k=0;k<KM;k++){
            a[i][j][k]=INTERIOR;
            T[i][j][k][0]=0.0;
            T[i][j][k][1]=0.0;
            if((i==0)|| (i==IM-1))a[i][j][k]=DIRICLET;
            if((j==0)|| (j==JM-1))a[i][j][k]=DIRICLET;
            if((k==0)|| (k==KM-1))a[i][j][k]=DIRICLET;
            if((i>0)&&(j>0)&&(i<IM-1)&&(j<JM-1)&&(k==0))a[i][j][k]=SURFACE;
        }
    }
}
```

In order to time-march from the initial condition we simply treat each node according to its attribute.

INTERIOR points are treated as follows:

```

case INTERIOR:
dQx=(T[i-1][j][k][n%2]+T[i+1][j][k][n%2]-2*T[i][j][k][n%2])*(K/(R*CP*DX*DX));
dQy=(T[i][j-1][k][n%2]+T[i][j+1][k][n%2]-2*T[i][j][k][n%2])*(K/(R*CP*DY*DY));
dQz=(T[i][j][k-1][n%2]+T[i][j][k+1][n%2]-2*T[i][j][k][n%2])*(K/(R*CP*DZ*DZ));
dT=DT*(dQx+dQy+dQz); /* only conduction, no sources */
T[i][j][k][(n+1)%2]=T[i][j][k][n%2]+dT;
break;

```

SURFACE points have an added laser heat input. Note the slightly different formulation for the Z-Heat flux:

```

case SURFACE:
dQx=(T[i-1][j][k][n%2]+T[i+1][j][k][n%2]-2*T[i][j][k][n%2])*K*DY*DZ/DX;
dQy=(T[i][j-1][k][n%2]+T[i][j+1][k][n%2]-2*T[i][j][k][n%2])*K*DX*DZ/DY;
dQz=(T[i][j][k+1][n%2]-T[i][j][k][n%2])*K*DX*DY/DZ+Q(i,j,k);
dT=DT*(dQx+dQy+dQz)/(R*CP*DX*DY*DZ);
T[i][j][k][(n+1)%2]=T[i][j][k][n%2]+dT;

```

Note the function $Q(i, j, k)$, which returns the heat input from the laser at each node. The solution procedure itself does not know if the laser moves or not. Laser motion is handled in the laser-power function by implementing a time-dependent heat source. the DIRICLET condition is very easy to treat. The code simply does nothing, and the corresponding temperature values remain as they were initially set:

```

case DIRICLET:
break;

```

This code can be used to solve both linear and non-linear heat diffusion problems. The non-linear solution is obtained by using time-dependent thermal conductivity and heat capacity.

4.6 Deposition

LCVD can be induced by either photolytic or pyrolytic decomposition of a metal-carrying precursor. The assumption will be made that the reaction is primarily pyrolytic, this being a necessary simplification. Under these conditions the rate at which

material is deposited is determined by the concentration of the reactants in the local microreaction zone and the local temperature. The local concentrations are the result of diffusion and convection of both reactants and products to and from the reaction zone, and the temperature is determined by the diffusion of the heat coming from the laser. Possible formation heats are not accounted for.

The local mass transport is not at all a trivial problem. As process parameters vary, different morphologies are observed due to spatially varying reactant concentrations. One of the more interesting such cases is the “volcano-shaped” cross section that has been observed in the literature and experimentally, which is most probably due to the onset of a diffusion-limited mass transport reaction regime. This phenomenon has been studied by Jensen ¹⁴ and co-workers who used a finite-element approach to obtain a solution to the transport-limited deposition problem. However, the effect of deposit morphology on the temperature distribution was assumed to be small and did not enter the calculation.

The rate of change of deposit height can be expressed as an exponential function of temperature, assuming an Arrhenius temperature dependence:

$$\frac{\partial h(x, y, t)}{\partial t} = Ae^{K_0(T/T_0)}$$

If the temperature distribution is assumed not to depend on to deposit morphology, a simple integration of h over time gives the deposit shape. This approach gives an order-of-magnitude estimate but it cannot reveal anything about possible mechanisms driving morphological features. The periodic instabilities that are observed when writing on low-conductivity substrates or the volcano-shaped cross-section seen for some power settings cannot be explained using this model.

To get a more accurate picture of the deposition both heat conduction along the deposit and mass transport to the reaction zone have to be considered. The full,coupled deposition, heat and mass transport problem is extremely difficult to solve, and

¹⁴ D.C. Skouby and K.F. Jensen, “Modelling of Pyrolytic laser-assisted chemical vapor deposition: Mass transfer and kinetic effects influencing the shape of the deposit”, *J. Appl. Phys.*

no such solution has been attempted in the literature. A simpler case, below the diffusion-limited growth limit, could be simulated for the purposes of this investigation and the results were found to conform with experiment.

The deposit was assumed to be thin, i.e. no temperature variations across the z direction. Actually, the solution was implemented as a 2D height field, $h(x, y)$ which was assumed to have the same temperature as the surface of the underlying substrate surface. The heatflow itself is affected by the height only because the deposited material has a different reflectivity than the substrate. The coupling between morphology and heatflow is only through the morphology-dependent heat input from the laser.

To summarize, the assumptions are:

- pyrolytic reaction
- uncoupled mass transport
- uniform reactant concentrations
- negligible heat of formation

The solution algorithm thus becomes:

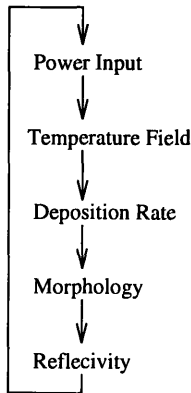


Figure 4.6 : The morphology-temperature coupling

The feedback loops outlined does not have to be stable, and in fact it is not. Experiment shows that for certain combinations of scanning speed, precursor pressure and/or laser power, stable, repetitive morphological structures occur that seem to be a physical manifestation of a limit cycle in such feedback processes:

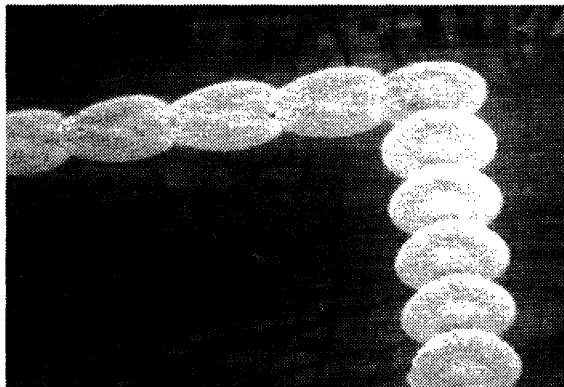


Figure 4.7: Platinum line written on polyamid substrate using a 120mW Argon laser at 50 $\mu\text{m/s}$

The periodic structures have been reported by a number of authors, and a number of hypotheses have been put forward to explain this phenomenon¹⁵. The explanation we think is most appropriate for the chemistries we investigated is a non-linear coupling between power input and deposit morphology via an almost discontinuous change in surface reflectivity as a function of deposit thickness. (see figure 4.8 for an explanation)



Periodical structures in metal LCVD : A Possible Mechanism

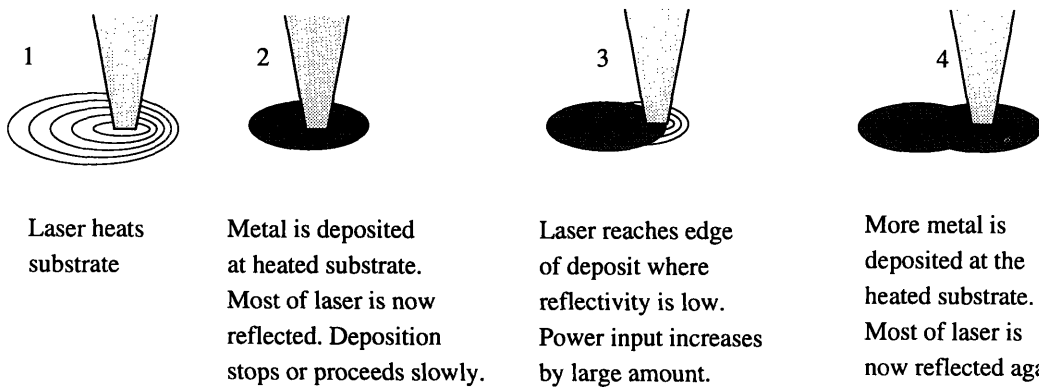


Figure 4.8 : The periodic structure

It seems that the mechanism is controlled by the relation between the deposit growth

¹⁵ For example, Y.C. Du, U.Kempfer, K. Piglmayer, and D. Bauerle: "New Types of Periodic Structures in Laser-Induced Chemical Vapor Deposition", *Appl. Phys. A* **39**, 167-171 (1986)

speed, i.e. the “spreading velocity” and the laser scanning velocity. If the metal spreads faster than the laser is scanned, the laser mostly heats substrate that is already covered with deposit, resulting in lower power input and thinner lines. If the laser moves faster than the spreading, most of the power is absorbed by clear substrate, which has a much lower reflectivity, and thermal diffusivity, so it tends to heat up faster, thus resulting in thicker lines. For scanning speeds that are smaller than the spreading speed for substrate heating, but larger than the spread speed for deposit heating, we get an instability that causes the deposition process to oscillate between the “substrate-heated” and the “deposit-heated” line length.

4.7 Deposition : Implementation

In order to implement the described deposition model, we a time-dependent heat source that is a function of deposit thickness. This is done as follows:

```
double Q(int i,int j,int k)
{
    double r,reflect;

    if(k!=0) return(0.0);
    r=sqrt((X(i)-SpotX)*(X(i)-SpotX)+(Y(j)-SpotY)*(Y(j)-SpotY));
    if(r>SPOTSIZE*1.5) return(0.0);
    reflect=1.0;
    if(D[i][j]>ReflectThreshold)reflect=DepositReflectivity;
    return(reflect*Qval*exp(1.0-r/SPOTSIZE));
}

void MoveQ()
{
    SpotX+=SpeedX*dt;
    SpotY+=SpeedY*dt;
    SpotZ+=SpeedZ*dt;
}
```

Where $Q(i,j,k)$ is called for every SURFACE node and $\text{MoveQ}()$ is called every time step.

The only other thing needed is to calculate the increment in deposit thickness due to

temperature at each SURFACE point. The deposit thickness is stored in $D[i][j]$, and it is used to calculate the non-linear reflectivity.

The deposition at each SURFACE node is calculated as follows:

```
XtraT=T[i][j][k][n%2]-Threshold;  
if(XtraT>0)D[i][j]+=DT*exp(XtraT);
```

The rate of deposition is an exponential function of temperature, and is non-zero only for temperatures above Threshold.

4.8 Deposition : Results

The simulation was run for a large number of boundary conditions in order to obtain a feel for the behavior of the model.

The model was constructed to verify the hypothesis that the periodic deposits observed are the result of a non-linear reflectivity-based process feedback. We therefore expect the numerical solution to exhibit periodicity for a narrow speed range and uniform deposit morphologies for all other speeds.

As far as geometrical dimensions are concerned, order-of-magnitude agreement with experimental results will be considered satisfactory in light of the significant simplifications of the presented model.

The data set used for a run was:

The density was taken to be 1.0

Heat capacity also 1.0

Thermal conductivity 1.0

X Length 1.0 with a discretization of 100

Y Length 0.3 with a discretization of 30

Z Depth 0.05 with a discretization of 5

Laser spotsize 0.03

Boundary temperature was taken 0
 Heat input 1.0 (or 5.0 for higher speeds)
 Deposition temperature threshold 100.0
 Reflectivity nonlinearity at deposit of height 0.01

The results clearly show the expected periodic form for a narrow velocity range and non-periodic straight deposits for all other velocities. Specifically, consider the runs for speeds of 50um/s, 120 um/s and 210 um/s, as shown in figure 4.9.

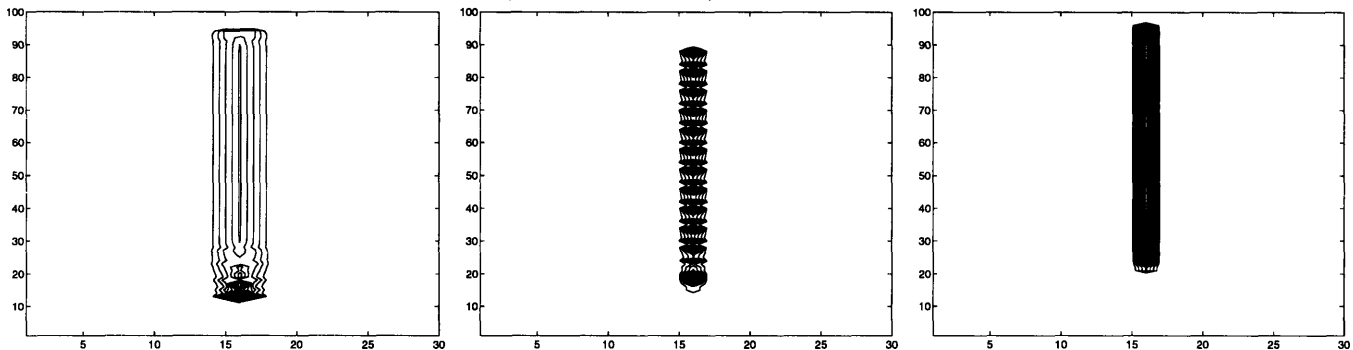


Figure 4.9 : Line Morphology for 50,120 and 250 um/s

It is clear that the periodic regime is bounded by non-periodic morphologies for both lower and higher speeds. Although the physical parameters used for this particular simulation are not corresponding to any real material, this run proves that the simple model considered is rich enough to behave in the experimentally observed manner. This is an indication that the hypothesis explaining the periodicity as a manifestation of a non-linearity in deposit reflectivity might be correct.

It is interesting to note that deposit periodicity seems to occur at a speed range that is greatly insensitive to the deposition thresholds and the deposit reflectivities. As soon as both velocities (i.e. heat diffusion and beam scan speed) are fixed, so is the regime of periodicity. A simulation varying thermal conductivity while keeping the other parameters constant was used to test this proposition.

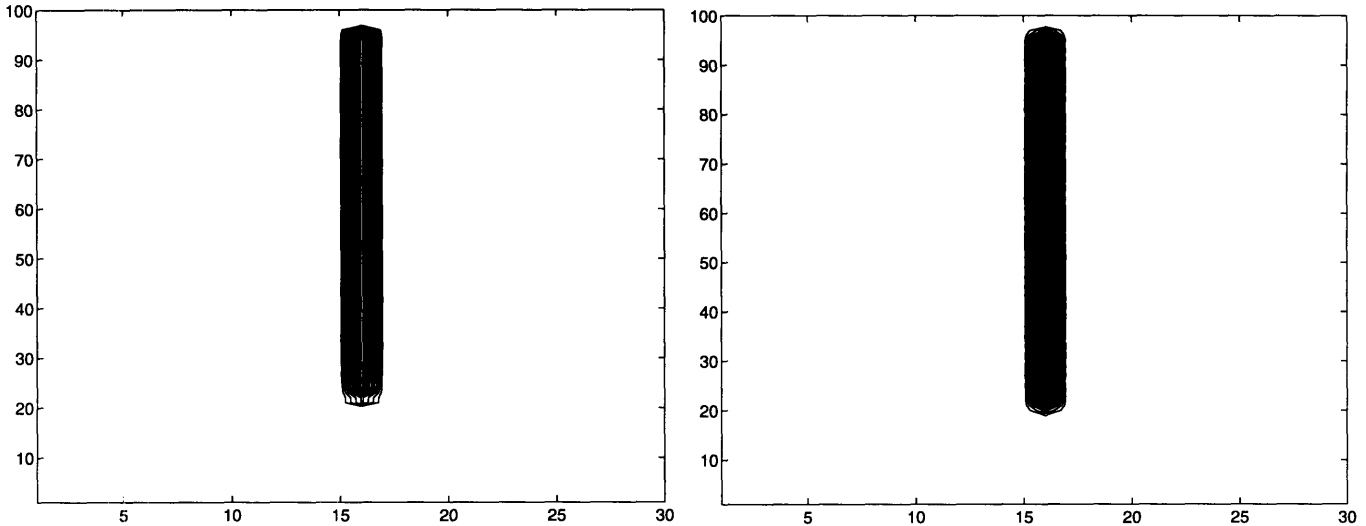


Figure 4.10 : Line Morphology for K = 1.0, 0.8 W/[KM]

The results further support the hypothesis that periodicity is closely linked to the relative magnitude of the three characteristic velocities of the system (diffusion at high power, diffusion at low power and laser scanning velocity).

4.9 The fully coupled case

The model can be extended to include direct coupling between morphology and heat diffusion by explicitly modeling the heat transfer through the deposited line. The easiest way to achieve this is to use a non-uniform, time-varying grid that matches deposit morphology. Deposit growth at the surface is then represented as increasing non-uniformity in the underlying discretization. In order to incorporate heat-conduction variations because of different material properties, we store conductivities for every node. As more and more metal is deposited, the averaged conductivity will converge to the bulk metal value. The additional data needed to implement this scheme are:

```
double T[IMAX][JMAX][KMAX][2];
double K[IMAX][JMAX][KMAX];      /* values for thermal conductivity */
double C[IMAX][JMAX][KMAX];      /* and heat capacity at every node */
double X[IMAX][JMAX][KMAX];      /* X,Y and Z cordinates of every   */
double Y[IMAX][JMAX][KMAX];      /* node (only Z changes over time, */
double Z[IMAX][JMAX][KMAX];      /* and that only for the top layer)*/
```

The redundancy of X and Y coordinates is not significant because the workstation has sufficient memory for all the data at the grid resolutions used. The bottleneck is computational speed and not storage capacity.

The deposition is then modelled as follows:

```

dZ=Z[i][j][k]-Z[i][j][k+1];
T[i][j][k][(n+1)%2]=T[i][j][k][n%2]+dT;
XtraT=T[i][j][k][n%2]-Threshold;
if(XtraT>0){
    dD=DT*exp(XtraT);
    K[i][j][k]=(dZ*K[i][j][k]+dD*Kd)/(dZ+dD); /* average thermal conductivity */
    Z[i][j][k]+=dD;                                /* alter grid spacing at surface */
}

```

Using this technique, deposition alters the discretization and the material properties that enter the heatflow calculation. A more accurate modelling would actually add nodes to the solution domain as the deposit grows. This is the methodology used to solve moving-boundary (Stefan) problems. Although this approach is the most promising one it goes beyond the goals of this investigation, which were to obtain a qualitative model to account for some of the experimental observations made during laser-assisted CVD.

Running the model just described results in periodic structures as expected, but for slightly different velocities and for a narrower velocity range. This means that the incorporation of heat diffusion across the deposit adds to the nonlinearity of the process, as expected.

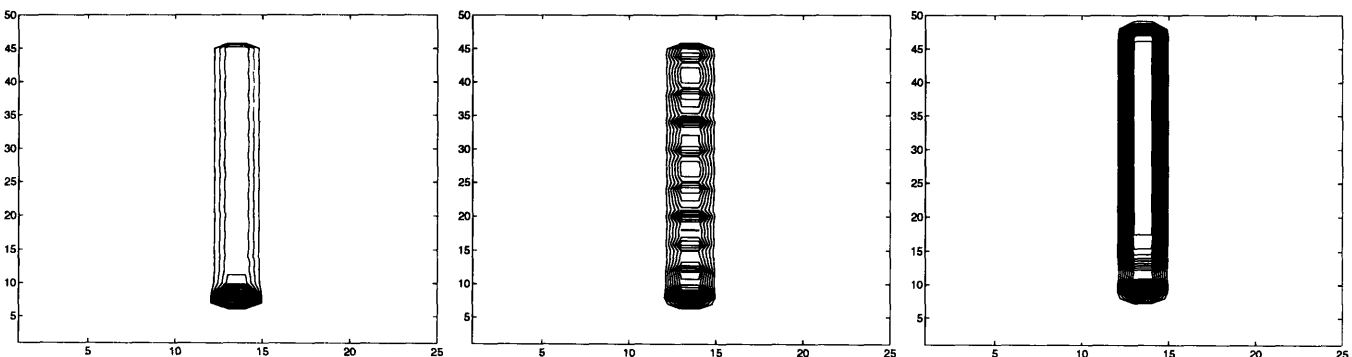


Figure 4.12 : Line Morphology for 120, 140 and 200 um/s

The temperature profile resulting from the coupling between morphology and heat diffusion is shown in figure 4.13. Note that the centerline of the deposit is colder than the surrounding substrate because of the deposit's higher thermal diffusivity.

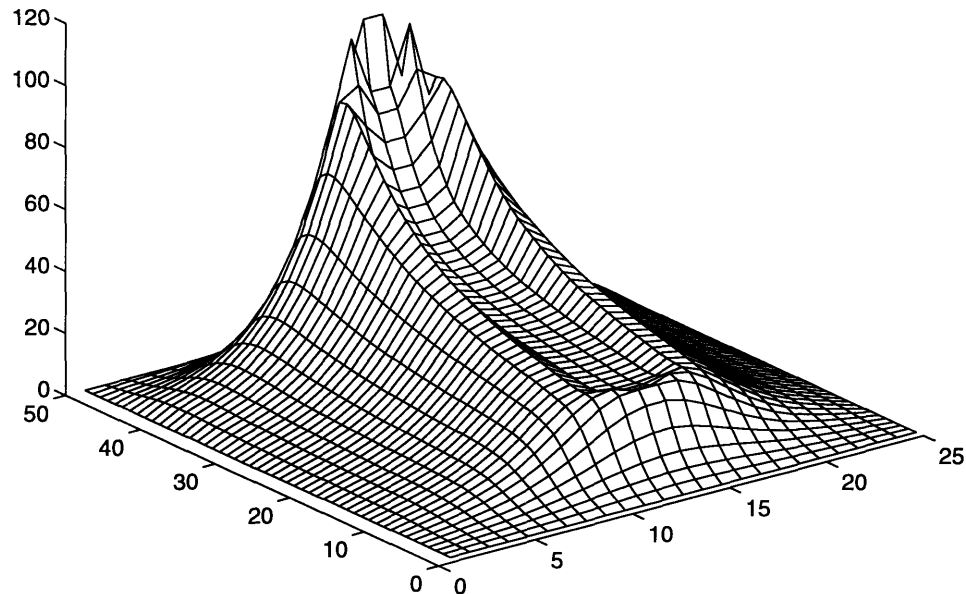


Figure 4.13 : Temperature field for the coupled
heatflow/morphology solution

4.10 Code Listing

```
*****
**
** unsteady 3D heat conduction from moving gaussian source
** into semi-infinite body of constant properties.
**
** Deposition rate proportional to temperature.
** Reflectivity is a non-linear step function.
**
**
** Derivation of the finite difference equation:
**
** dQx = (dQx+) + (dQ-) (heat loss to both directions)
**
** dQx+ = (T[i+1] - T[i]) * k * A / L = ( T[i+1] - T[i] ) * K * DY * DZ / DX
** dQx- = (T[i-1] - T[i]) * k * A / L = ( T[i-1] - T[i] ) * K * DY * DZ / DX
**
** dQx = (T[i+1] + T[i-1] - 2T[i]) * K * DX * DZ / DX
**
** dQ = dQx + dQy + dQz
**
** but : dQ = r * Cp * dV * dT = r * Cp * DX * DY * DZ
**
** so : dT = DT * dQ / ( r * Cp * DX * DY * DZ )
**      = DT * ( T[i+1][j][k] + T[i-1][j][k] -
**                  2*T[i][j][k] ) * K / ( R * CP * DX * DX )
**      = DT * ( T[i][j+1][k] + T[i][j-1][k] -
**                  2*T[i][j][k] ) * K / ( R * CP * DY * DY )
**      = DT * ( T[i][j][k+1] + T[i][j][k-1] -
**                  2*T[i][j][k] ) * K / ( R * CP * DZ * DZ )
**
**
** and R is the density, CP the specific heat, K the thermal conductivity
**
** and T[n+1] = T[n] + dT, an explicit scheme
**
*****
#include <stdio.h>
#include <math.h>

/*
** Constants
*/
#define PI 3.1415926536
```

```

#define TRUE 1
#define FALSE 0

/*
** Attribute values
*/
#define INTERIOR 0
#define DIRICLET 1
#define NEUMANN 2
#define SURFACE 9

/*
** Grid Size
*/
#define IM 100
#define JM 30
#define KM 5

/*
** Solution
*/
double T[IM][JM][KM][2];
double D[IM][JM];
char a[IM][JM][KM];

/*
** Material Properties [SI units]
*/
#define R 1.0
#define CP 1.0
#define K 1.0

/*
** Slab Geometry in [m]
*/
#define H 1.0
#define LX 1.0
#define LY 0.3
#define LZ 0.05
#define SPOTSIZE 0.03

/*
** Deposition Process Parameter
*/
#define RATE 0.1

/*
** Discretization

```

```

*/
#define DX  (LX/IM)
#define DY  (LY/JM)
#define DZ  (LZ/KM)
double DT=0.00001;           /* time step, in [sec] */

#define X(i)  (((double)i)*DX)          /* grid i -> x-coordinate */
#define Y(j)  (((double)j)*DY)          /* grid j -> y-coordinate */
#define Z(k)  (((double)k)*DZ)          /* grid k -> z-coordinate */

/*
** Process Parameters
*/
double Qval=1.0;
double Threshold=10.0;
double DepositReflectivity=0.1;
double ReflectThreshold=1000.0;

/*
** Laser motion
*/
#define SPEED 1000.0

double SpotX=LX/10;
double SpotY=LY/2;
double SpotZ=0;

double SpeedX=SPEED;      /* in units/time step */
double SpeedY=0.0;
double SpeedZ=0.0;

/*
** Control Values
*/
int SaveStep=50;

char OutFile[80];

/***********************/

void Parse(int argc,char **argv)
{
    int i;
    strcpy(OutFile,"res.dat");
    if(argc<2) return;
}

```

```

for(i=1;i<argc;i++)if(argv[i][0]=='-')switch(argv[i][1]|32){
    case 's': SaveStep=atoi(&argv[i][2]);
                break;
    case 't': DT=atof(&argv[i][2]);
                break;
    case 'q': Qval=atof(&argv[i][2]);
                break;
    case 'y': Threshold=atof(&argv[i][2]);
                break;
    case 'u': SpeedX=atof(&argv[i][2]);
                break;
    case 'r': DepositReflectivity=atof(&argv[i][2]);
                break;
    case 'e': ReflectThreshold=atof(&argv[i][2]);
                break;
    case 'f': strcpy(OutFile,&(argv[i][2]));
                break;
}

}

/*****



/*
**
** attribute values, initial conditions, guess
**
*/
void SetUp()
{
    int i,j,k;
    for(i=0;i<IM;i++)for(j=0;j<JM;j++){
        D[i][j]=0;
        for(k=0;k<KM;k++){
            a[i][j][k]=INTERIOR;
            T[i][j][k][0]=0.0;
            T[i][j][k][1]=0.0;
            if((i==0)|| (i==IM-1))a[i][j][k]=DIRICLET;
            if((j==0)|| (j==JM-1))a[i][j][k]=DIRICLET;
            if((k==0)|| (k==KM-1))a[i][j][k]=DIRICLET;
            if((i>0)&&(j>0)&&(i<IM-1)&&(j<JM-1)&&(k==0))a[i][j][k]=SURFACE;
        }
    }
}

/*****

```

```

**
** The moving source.
*/
int n=0;           /* iteration count */

/*
**
**
**
*/
double Q(int i,int j,int k)
{
    double r,reflect;

    if(k!=0) return(0.0);
    r=sqrt((X(i)-SpotX)*(X(i)-SpotX)+(Y(j)-SpotY)*(Y(j)-SpotY));
    reflect=1.0;
    if(D[i][j]>ReflectThreshold)reflect=DepositReflectivity;
    return(reflect*Qval*exp(1.0-r/SPOTSIZE));
}

/*
**
** Move source
**
*/
void MoveQ()
{
    SpotX+=SpeedX*DT;
    SpotY+=SpeedY*DT;
    SpotZ+=SpeedZ*DT;
    printf("Spot at %3.1lf %3.1lf\n",SpotX/DX,SpotY/DY);
}

/***********************/
/*
**
** display functions
**
*/
int max(int a,int b){ return(a>b?a:b); }

int min(int a,int b){ return(a>b?b:a); }

double ShowSlice()

```

```

{
    int i,j,k;
    int l;
    double r,max;
    FILE *fp;

    printf("\n");
    if((fp=fopen(OutFile,"w"))==NULL)puts("Error!");
    rewind(fp);
    printf("Output state to [%s]\n",OutFile);
    for(i=0;i<IM;i++){
        for(j=0;j<JM;j++){
            fprintf(fp,"%1.2lf ",D[i][j]);
        }
        fflush(fp);
    }
    fprintf(fp,"\n");
}
fclose(fp);
}

main(int argc,char **argv)
{
    int i,j,k;          /* counters */
    double err,lerr;    /* errors */
    int ierr,jerr,kerr;

    double dQx,dQy,dQz; /* temperature differences */
    double dT,dQ,XtraT;

    Parse(argc,argv);
    SetUp();
    n=0;
    do{
        err=0;
        ierr=jerr=0;
        /** Move Laser **/
        MoveQ();
        /** Time-march heat conduction **/
        for(i=0;i<IM;i++)for(j=0;j<JM;j++)for(k=0;k<KM;k++)switch(a[i][j][k]){
            case INTERIOR:
                dQx=(T[i-1][j][k][n%2]+T[i+1][j][k][n%2]-2*T[i][j][k][n%2])*(K/(R*CP*DX*DX))
                dQy=(T[i][j-1][k][n%2]+T[i][j+1][k][n%2]-2*T[i][j][k][n%2])*(K/(R*CP*DY*DY))
                dQz=(T[i][j][k-1][n%2]+T[i][j][k+1][n%2]-2*T[i][j][k][n%2])*(K/(R*CP*DZ*DZ))
                dT=DT*(dQx+dQy+dQz); /* only conduction, no sources */
                if(fabs(dT)>err){
                    err=fabs(dT);
                    ierr=i;
                }
            }
        }
    }
}

```

```

        jerr=j;
        kerr=k;
    }
    T[i][j][k][(n+1)%2]=T[i][j][k][n%2]+dT;
    break;

    case SURFACE:
dQx=(T[i-1][j][k][n%2]+T[i+1][j][k][n%2]-2*T[i][j][k][n%2])*K*DY*DZ/DX;
dQy=(T[i][j-1][k][n%2]+T[i][j+1][k][n%2]-2*T[i][j][k][n%2])*K*DX*DZ/DY;
dQz=(T[i][j][k+1][n%2]-T[i][j][k][n%2])*K*DX*DY/DZ+Q(i,j,k);
dT=DT*(dQx+dQy+dQz)/(R*CP*DX*DY*DZ);
if(fabs(dT)>err){
    err=fabs(dT);
    ierr=i;
    jerr=j;
    kerr=k;
}
T[i][j][k][(n+1)%2]=T[i][j][k][n%2]+dT;
XtraT=T[i][j][k][n%2]-Threshold;
if(XtraT>0)D[i][j]+=DT*exp(XtraT);
break;

    case NEUMANN:
        break;
    case DIRICLET:
        break;
    default:
        break;
}
n++;
printf("#%d @(%d,%d,%d) Err=%lf T=%lf D=%lf (%lf %lf)\n",n,ierr,jerr,kerr,err,T[ierr]
if((n%SaveStep)==0)ShowSlice();
}while(1);
}

```

Chapter 5

Conclusions

5.1 Summary

A laser-driven microchemistry system for modification, trimming or fabrication of microelectronic and micromechanical devices was demonstrated. Specifically we demonstrated one-step connect, disconnect, via formation and trimming applications.

In order to better understand the deposition process we developed a simple numerical model to explain an unexpected periodic structure observed for certain process parameters.

Metallization writing rates for 1- to 5- μm -thick conductors were found to be from 50 to 1000 $\mu\text{m}/\text{s}$. Resistivities are typically 3-15 $\mu\Omega \text{ cm}$ for many metals (e.g. Pt, Al, Cu, Au, W, and Co). The range of processes was extended to include metallurgies for multichip modules and microelectromechanical devices (MEM).

The system was constructed to be consistent with these capabilities. Two-dimensional, X-Y, motion is servo-controlled to 0.15 μm resolution over a 6-inch range of travel; Z is servo-controlled to 0.1 μm . Three-axis motion is synchronized with laser operations by means of a dedicated microprocessor. Laser parameters and motion paths are specified on a live video image of the workpiece by means of an interactive graphical user interface. Three-dimensional contouring is achieved by approximating the

spot trajectory as a sequence of X-Y-Z target points connected by linear, constant velocity motion paths. Laser power, repetition rate and scan velocity can be varied as the path is traversed. Proper workpiece alignment is and process repeatability are achieved with image-based positioning and calibration algorithms.

We conducted a series of demonstrations on integrated circuits (ICs), multichip modules (MCMs) and MEM devices. We found that the high resolution is essential for ICs, while the three dimensional capability is needed for MCMs and MEMs. Laser-deposited copper, aluminum, platinum and gold conductors have been developed. The processes permit real-time writing of interconnection for circuit configuration, rework, chip bondout, testing and systems engineering. Recent process extensions now permit operation on MCM metallurgies including all silicon, ceramic, and advanced deposited layer or laminate technologies. Collaborative demonstrations have been completed with several MCM foundries. The technology was found to provide (1) a low-cost rework option, (2) reversible interconnect for module testing, (3) means to implement redundancy and universal substrate options, and (4) means to trim terminations and other circuit parameters. In the MEM application, real-time tuning of device parameters under live test has been demonstrated.

5.2 References

1. H.S. Carslaw and J.C. Jaeger, *Conduction of Heat in Solids* (Oxford U.P., New York, 1959)
2. J. Hill and J.N. Dewynne, *Heat Conduction* (Blackwell Scientific Publications, 1987)
3. H.E Cline and T.R. Anthony, *J. Appl. Phys.* **48**, 3895 (1977)
4. M.Lax, "Temperature rise induced by a laser beam", *J. Appl. Phys.* **48**, 3919 (1977)
5. M.Lax, "Temperature rise induced by a laser beam II. The nonlinear case", *Appl. Phys. Lett.* **33**, 786 (1978)
6. Robert J. Harrach, "Analytical solutions for laser heating and burnthrough of opaque solid slabs", *J. Appl. Phys.* **48**, 2370 (1977)
7. J.E. Moody and R.H. Hendel, "Temperature profiles induced by a scanning cw laser beam", *J. Appl. Phys.* **53**, 4634 (1982)
8. G. Garrido, B. Leon and M. Perez-Amor, "A model to calculate the temperature induced by a laser", *J. Appl. Phys.* **69**, 1133 (1991)
9. Y.I. Nissim, A.Lietoila, R.B. Gold and J.F. Gibbons, " Temperature distributions produced in semiconductors by a scanning elliptical or circular cw laser beam", *J. Appl. Phys.* **51** 274 (1980)
10. J.Mazumder and W.M.Steen, "Heat transfer model for cw laser material processing", *J. Appl. Phys.* **51**, 941 (1980)
11. D.C. Skouby and K.F. Jensen, "Modelling of pyrolytic laser-assisted chemical vapor deposition: Mass transfer and kinetic effects influencing the shape of the deposit", *J. Appl. Phys.* **63**, 198 (1988)

12. A. Kar, M. N. Azer and J. Mazumder, "Three-dimensional transient mass transfer model for laser chemical vapor deposition of titanium on stationary finite slabs", *J. Appl. Phys.* **69**, 757 (1991)
13. Y. Zeiri, U. Atzmony and J. Bloch, "Monte Carlo simulation of laser induced chemical vapor deposition", *J. Appl. Phys.* **69**, 4110 (1991)
14. N. Kirichenko, K. Piglmeyer and D. Bauerle, "On the Kinetics of Non-Equimolecular Reactions in Laser Chemical Processing", *Appl. Phys. A* **51**, 498 (1990)
15. D. Bauerle, B. Luk'yanchuk, and K. Piglmayer, "On the Reaction Kinetics in Laser-Induced Pyrolytic Chemical Processing", *Appl. Phys. A* **50** 385 (1990)
16. N. Arnold, R. Kullmer and D. Bauerle, "Simulation of growth in pyrolytic laser-CVD of microstructures-I. One-dimensional approach", *Microelectronic Engineering*. **20**, 31 (1993)
17. N. Arnold and D. Bauerle, "Simulation of growth in pyrolytic laser-CVD of microstructures-II. Two-dimensional approach", *Microelectronic Engineering*. **20**, 43 (1993)
18. Y.C. Du, U. Kempfer, K. Piglmayer, and D. Bauerle, "New Types of Periodic Structures in Laser-Induced Chemical Vapor Deposition", *Appl. Phys. A* **39** 167-171 (1986)
19. Z. Toth, P. Kargl, C. Grivas, K.Piglmeyer, T.Szorenyi and D. Bauerle, "LCVD of Tungsten Microstructures on Quartz", *Appl. Phys. B.* **54**, 189 (1992)
20. D.J. Ehrlich, J.Y. Tsao (eds.): *Laser Microfabrication - Thin Film Processes and Lithography* (Academic, New York 1989)
21. O.Conde, A.Kar and J. Mazumder, *J. Appl. Phys.* **72**, 754 (1992)
22. Y. Mosishige, S. Kitamura and S. Kishida, *Applied Surface Science.* **46**, 108 (1990)

23. S.D. Allen, *J. Appl. Phys.* **52**, 6501 (1981)
24. D. Bauerle: *Laser Processing and Diagnostics* (Springer, Berlin 1984)